Chapter 2
Electron Beam Irradiation Effects and In-Situ Irradiation of Nanomaterials

Tao Xu, He Zheng, Jianbo Wang, Florain Banhart, and Litao Sun

2.1 A Brief History of In-Situ Electron Irradiation

The transmission electron microscope (TEM) is capable of directly imaging the atomic structure of the specimen, which has become an indispensable tool to obtain atomic-level information and establish the relationship between structure and properties [1]. It is well known that the formation of an image in the TEM requires the elastic interaction of the object with an energetic electron beam (typically 60–300 keV, in a few instruments up to 1–3 MeV), raising a natural problem of electron irradiation. In fact, the interaction of the incident electrons with atomic nuclei or electrons surrounding the nuclei can cause temporary or permanent changes in the structure and/or the chemistry of the specimen, which is often referred to as electron irradiation damage [2]. Such damage has already been perceived in the early days of TEM [3] and is usually undesirable in TEM studies because radiation artifacts may appear in the images. Still today, radiation damage remains a fundamental difficulty and limits the applicability of TEM in the study of certain materials. Considering that the amount of radiation damage is proportional to the accumulated electron dose [2], beam-induced changes is more obvious in *in situ* experiments, where the specimen is inevitably exposed to electron bombardment for an extended period to allow the

T. Xu · L. Sun (✉)
Key Lab of MEMS of Ministry of Education, SEU-FEI Nano-Pico Center, Southeast University, Nanjing 210096, P. R. China
e-mail: slt@seu.edu.cn

H. Zheng · J. Wang
School of Physics and Technology, Center for Electron Microscopy, MOE Key Laboratory of Artificial Micro- and Nano-Structures, and Institute for Advanced Studies, Wuhan University, Wuhan 430072, P. R. China

F. Banhart
Institut de Physique Et Chimie Des Matériaux, UMR 7504, CNRS, Université de Strasbourg, 67000 Strasbourg, France

recording of transformations in time [4–6]. Separating electron irradiation effects from the analysis of the desired observations requires a detailed understanding of fundamental damage mechanisms.

Although radiation damage in the TEM is known since the 1940s [3], electron irradiation effects haven't become a subject of intense research until the 1960s, when electron irradiation in the TEM was widely used to simulate particle irradiation in nuclear fission or fusion reactor materials [7–9]. The particular advantage of *in situ* irradiation experiments is that the evolution of radiation defects can be observed directly in real time. It should be noticed that the electrons causing structural alterations and the electrons for imaging are usually not the same. But they stem from the same beam that can be used for both at the same time. With a continuous improvement of spatial resolution, TEM has enabled us to study radiation effects on the atomic scale since the 1980s [10]. Nowadays, aberration-corrected instruments promise further advance in this direction as the rearrangement of individual atoms in two-dimensional (2D) sheets of monoatomic thickness becomes visible without any overlap of other atom layers and projection artifacts in the image [11–13]. A large number of different radiation phenomena have been experimentally identified, ranging from atom displacements to electronic excitations. The main effects can be categorized into electron–nucleus scattering (atom displacement and sputtering) and electron–electron scattering events (electrostatic charging, radiolysis, or electron beam heating).

It is known that different damage mechanisms can be correlated with each other and depend on the material. Generally, inelastic electron–electron scattering can cause severe difficulties in the studies of insulators, ionic crystals, and organic materials [14–16] but is unimportant for metallic materials due to the presence of conduction electrons. Elastic electron–nucleus scattering can sometimes be neglected in insulating or organic specimens when the displacement cross section is lower than the excitation or ionization cross section. By contrast, electronic effects are quenched in conducting specimens where radiation damage is essentially restricted to atom displacements [17].

It is important to point out that electron irradiation is not only damaging specimens but also beneficial in *in situ* experiments to explore thermal nonequilibrium phenomena and the dynamic behavior of atomic defects, reveal the physics behind novel phenomena at the atom scale, and extend the applicability of electron irradiation. This chapter focuses on the variety of electron irradiation-induced processes where the electron beam triggers and drives the dynamic behavior of materials while in several cases some other excitations (such as heating) may be applied to the specimen at the same time.

As early as the late 1940s, electron beams in TEM had been intentionally used to trigger structural transformations in ionic crystals [18] and organic pigments [19], followed by the study of electron irradiation-induced decompositions in the early 1950s [20]. Due to the low spatial resolution in this period, electron diffraction always had to be used to confirm the formation of irradiation-induced phases. Over the same period, electron beam-induced deposition of carbonaceous residue of hydrocarbons

or other organic molecules has shown the capability to fix the specimen and partly protect the specimen from chemical attacks or electron bombardment [21].

Driven by the needs of nuclear power industry, electron irradiation in the TEM was widely applied to the study of structural stability of reactor materials under electron bombardment in the 1960s and 1970s [22], enabling the development of materials that are robust under neutron irradiation in the reactor. However, electron irradiation-induced point defects were not visible in the TEM at that time except they appeared in agglomerates or secondary defects such as dislocation loops, voids, and precipitates or induced observable structural changes of other defects. Consequently, electron irradiation-induced nucleation, growth or migration of dislocations [23], crystalline-amorphous transformations [24], and precipitation [25] begun to attract increasing attention. At the same time, electron beam flashing became a well-established technique to prepare thin crystal specimens with clean surfaces [26].

Electron irradiation-induced deposition became also of interest when gaseous precursors could have continuously flowed into the specimen chamber without considerable loss of spatial resolution [27]. Gas molecules may be ionized by the electron beam, making the molecules more reactive to interact or etch solid materials. Even without gas precursors, adatoms generated by electron irradiation can migrate and deposit within some areas of the object, resulting in the formation of novel structures [28]. Since the 1970s, computer-controlled electron beam-induced deposition and etching performed inside the TEM has become a productive technique to fabricate nanostructures [29].

Almost all subjects mentioned above have been studied again with atomic resolution since the 1980s when the spatial resolution of modern TEMs was promoted to the scale of 0.1 nm or even below. Many unexpected phenomena and novel effects were discovered in nanomaterials under electron irradiation [30]. For instance, spherical carbon particles showed self-compression under electron beam irradiation at high temperature, resulting in the nucleation and growth of diamond crystals [31]. The electron beam in TEMs with an aberration corrector can be focused onto spots of less than 0.1 nm which offer the possibility to fabricate and modify the specimen on the scale of few or even single atoms [32]. Besides, environmental specimen stages with liquid cells are used intensively in the last 15 years, and the interaction between the electron beam and the solution may induce reactions and produce species which play an important role in the observed nucleation and growth behaviors of nanocrystals in solution [33].

2.2 Fundamental Electron Irradiation Effects

In an electron microscope, the specimen is exposed to energetic electron bombardment during observation. As a low-mass particle, the electron can easily be deflected by the Coulomb interactions with the atomic nucleus or/and electrons in the specimen. The electron scattering can be categorized into elastic events without energy

loss and inelastic events with energy loss of the electrons. Elastic scattering represents electrostatic deflection by the Coulomb field of each atomic nucleus, which gives rise to electron diffraction patterns and to contrast in TEM images; inelastic scattering represents Coulomb interaction with the electrons surrounding the nucleus, which can generate several types of excitations in the specimen, and these signals can be used for elemental analysis in TEM [34]. However, these processes can also cause temporary or permanent changes in the structure and/or the chemistry of the specimen. For instance, electron–nucleus scattering can lead to atom displacements in the bulk of the specimen or sputtering of atoms from its surface, while electron–electron scattering can result in ionization, electrostatic charging, radiolysis, heating, and deposition [2]. Generally, displacement damage increases, whereas ionization damage decreases with increasing incident electron energy. An optimum accelerating voltage should be chosen to minimize the combined radiation damage depending on the materials to study.

2.2.1 Atom Displacements

A displacement event occurs by the direct transfer of the kinetic energy of the electrons to atoms in the solid via electron–nucleus collisions, knocking them out of their atomic sites and thereby degrading the crystalline perfection. It is the primary radiation damage mechanism in specimens with conduction electrons. Taking into account the energy and momentum conservation, only little energy E can be transferred from the incident electron to the nucleus, and the energy depends on the deflection angle θ:

$$E = E_{\max} \sin^2\left(\frac{\theta}{2}\right), \tag{2.1}$$

where E_{max} is the maximum energy transferred by a head-on collision ($\theta = 180°$). It is a function of the incident-electron energy E_0:

$$E_{\max} = \frac{2E_0(E_0 + 2m_e c^2)}{Mc^2}, \tag{2.2}$$

where m_e is the electron mass, M is the mass of the nucleus, and c is the speed of light. It is intuitively clear that head-on collisions are less likely than high-angle scattering [35].

If E exceeds displacement threshold energy E_d, the atom can be displaced to an interstitial position so that a vacancy–interstitial pair is created which does not spontaneously recombine. The migration of existing vacancies and interstitials can be promoted by electron irradiation even if the transferred energy is below E_d. Such a radiation-induced diffusion has qualitatively the same effect as thermal diffusion [35]. Generally, E_d (the energy of the displaced atom) is above 10 eV for atoms

in most bulk crystals and is characteristic of the material depending on its chemical composition and crystal structure. For instance, E_d of carbon in diamond is obviously larger than that in graphite, and the value along the hexagonal axis is evidently smaller than along the basal plane in graphite; atoms at grain boundaries or other structural defects are also displaced more easily because of their lower binding energy [35].

The displacement rate p, which states how often each atom is displaced per second, is given by

$$p = \sigma J, \tag{2.3}$$

where σ is the displacement cross section and J is the beam current density which typically ranges between 10 A/cm^2 in high-resolution imaging in a typical TEM and 10^4 A/cm^2 with the fully focused electron beam on the specimen. For light elements, σ can be an approximation calculated by the McKinley–Feshbach formalism [36]:

$$\sigma = \frac{4Z^2 E_R^2}{m_e^2 c^4} \left(\frac{E_{\max}}{E^d} \right) \pi a_0^2 \left(\frac{1-\beta^2}{\beta^4} \right) \left\{ 1 + 2\pi\alpha\beta \left(\frac{E_d}{E_{\max}} \right)^{1/2} \right.$$
$$\left. - \frac{E_d}{E_{\max}} \left[1 + 2\pi\alpha\beta + (\beta^2 + \pi\alpha\beta)\mathrm{In}\left(\frac{E_{\max}}{E_d} \right) \right] \right\} \tag{2.4}$$

where Z is the atomic number of the displaced atom, E_R is the Rydberg energy, a_0 is the Bohr radius of the hydrogen atom, $\beta = v/c$, and $\alpha = Z/137$. It should be noticed that this equation is suitable to evaluate the total displacement cross section for static atoms. If the effect of atomic vibrations is taken into account, the maximum transferred energy E_{max} has to be replaced by a function containing the atom vibration and incident electron energy E_0 [37]. Such a modification just smoothens the cross section at the onset without changing the trend.

Normally, the cross section increases rapidly above the threshold E_{thr} (value of E_0 above which displacement occurs, which can be obtained by setting $E_{max} = E_d$ in Eq. 2.2, normally larger than tens of keV), and reaches its maximum value at about twice the threshold and decreases again at higher energy due to relativistic effects [35]. Assuming the atoms are hard spheres, the displaced atoms may cause further displacements when $E_{max} \geq 2E_d$. Such displacement cascades are of importance in larger objects where the total cross section may increase with the electron energy even at high electron energy [35].

The only way to avoid atom displacements is to use an electron energy below E_{thr} for microscopy. If the energy cannot be achieved experimentally, lowering the beam current and shortening the illumination time as much as possible should be considered to reduce displacement damage.

2.2.2 Surface Sputtering

If high-angle elastic scattering occurs at a surface atom, the atom can easily leave the specimen due to the open space above the surface, which is known as sputtering. It is obvious that sputtering primarily occurs on the beam-exit surface because the momentum transfer in a high-angle scattering is mainly along the incident direction [2].

Equations 2.1–2.4 remain valid but the sputtering threshold energy E_s for surface atoms is much lower as they are less tightly bound than bulk atoms [34], as shown in Table 2.1. E_s is often taken as the sublimation energy E_{sub} as well as the values between E_{sub} and $2E_{sub}$ [38]. Almost all low-Z and medium-Z atoms can be knocked away from the surface by 300 keV electrons, which means that the morphology of the specimen can be modified in a controllable manner in this way. Similar to displacement damage, the strategy for avoiding sputtering is to use a low electron energy and to limit the accumulated radiation dose. Besides, coating a thin layer of carbon onto the specimen surface may prevent sputtering damage.

It is a remarkable fact that most displaced atoms at the surface diffuse on the surface as adatoms and do not leave the specimen immediately. These atoms are weakly bound to the surface by physisorption or/and chemisorption and can be further sputtered if the transferred energy exceeds the adsorption energy E_{ad}. Surface diffusion is facilitated because the activation energy E_{sd} is typically lower than E_{ad} by a factor of 3 or more [39]. In this perspective, it is understandable that sputtering-induced rough surfaces tend to anneal under electron beam irradiation if the beam-induced surface migration is sufficient to fill the vacant sites. However, it is hard to quantify adatom motion because the structure of the surface is often unknown. Atomic steps, water molecules, or hydrocarbon contamination on the surface can affect adatom diffusion [39].

Table 2.1 Comparison of the maximum transferred energy E_{max} at 300 keV with displacement threshold energies E_d and sputtering threshold energies E_s [34]

Element	E_{max} (eV)	E_d(eV)	E_s (eV)	Element	E_{max} (eV)	E_d(eV)	E_s (eV)
Al	31.6	16	4–8	Ti	17.8	15	4–8
V	16.72	29	7–14	Cr	16.38	22	5–11
Fe	15.25	16	4–8	Co	14.45	23	5–12
Ni	14.5	22	6–11	Cu	13.4	18	4–9
Zn	13.03	16	4–8	Nb	9.17	24	6–12
Mo	8.88	27	7–14	Ag	7.90	28	7–14
Cd	7.58	20	5–10	Ta	4.71	33	8–16
Pt	4.37	33	8–16	Au	4.32	36	9–18

2.2.3 Electrostatic Charging

Electrostatic charging occurs primarily in electrically insulating specimens due to the lack of conductivity to neutralize the local charge. Under normal conditions, the irradiated area charges positively due to the emission of secondary and Auger electrons. The net charge accumulated by the specimen per second depends both on the backscattering coefficient η and the yield for secondary electrons δ. For thin TEM specimens, the steady-state condition represents an equilibrium between the electrical currents [2]:

$$I - I_t + V_s/R_s = I\eta + I\delta(V_s), \tag{2.5}$$

where I is the incident electron current, I_t is the transmitted electron current, V_s is the surface potential developed in the beam, and R_s is the effective electrical resistance between the irradiated and the surrounding regions of specimen. The terms on the left-hand side represent currents entering the irradiated area, while the right-hand side represents the loss of current by backscattering and by secondary emission. In view of the fact that very few electrons from the beam are absorbed in a thin specimen, I_t approaches I, causing V_s to be positive, especially at high E_0. In addition, electrostatic charging can also occur via the Knotek–Feibelman (K–F) mechanism in which Auger electrons lead to a positive charge buildup [2].

At high current density, V_s may be dozens of volts [40]. This voltage can lead to an ultra-high electrical field of up to 10^{10} V/m at the edge of the illuminated area, which may cause an electrical breakdown in the insulating specimen and ion migration in the lateral direction [41]. In addition, electrostatic charging can also produce a mechanical force, which may even cause rupture of thin films [2].

Good conductive contacts between the specimen and the support or specimen holder can reduce charging, therefore reducing electron beam irradiation-induced charging effects.

2.2.4 Radiolysis

Radiolysis is the beam-induced ionization of atoms or breaking of chemical bonds by electron–electron scattering which may lead to a locally modified chemistry of the sample under the beam. Radiolysis is of significance in insulators (such as halides, oxides, hydroxides, sulfides, silicates, and so on) where inelastic scattering can cause local irreversible bond breaking and even mass loss. For alkali halides, which are a class of radiation-sensitive inorganic materials, the decay of exciton states leads to the formation of double-halogen ions and anion vacancies. Then the vacancies aggregate to form voids, while the halogen ions may condense to create dislocation loops and diffuse to the surface, eventually followed by halogen loss.

In the case of transition metal oxides, radiolysis may involve considerable electrostatic charging. The Auger decay of the inner-shell vacancy states in the metal atoms leads to positively charged O atoms, which can be ejected from the surface due to the electrostatic repulsion of the surrounding metal ions, thus leaving a metal-rich surface [42]. Such a process does not stop till the specimen surface becomes sufficiently conductive to screen the positive charge.

Radiation damage in organic solids is generally more extensive. Amorphous polymers or molecular crystals consist of strong covalent bonds and weak non-covalent bonds. Non-covalent bonds are easily broken followed by structural changes and displacements of molecules, resulting in crystallinity degradation and even mass loss [43]. Normally, aromatic compounds are much stable than aliphatic compounds due to their ring structures with π electrons which allows the deposited energy to be dissipated within the π electron pool without bond breakage [44].

The radiolysis of liquid solutions had attracted growing attentions, especially with the development of liquid cell TEM [33]. Considering that most solutions used in liquid cell TEM experiments have low concentrations of solutes, inelastic scattering in the liquid causes primarily radiolysis of the solvent. Radiolysis in both aqueous and organic solvents is applied to establish oxidizing or reducing environments, which is the basis for studying nucleation, growth, and degradation [45]. When water molecules interact with incident electrons, they decompose into strongly reducing solvated electrons e_h^-, hydrogen radicals $H^\bullet$, and oxidizing hydroxyl radicals $OH^\bullet$. Then these initial products diffuse and participate in further reactions to yield reactive products, including H_2, O_2, H_2O_2, H_3O^+, $HO_2^\bullet$, and so on [33]. These radicals will change the chemical environment but their concentration reaches an equilibrium within a very short time; furthermore, the radiolysis of water may alter the solution's PH because of the presence of H_3O^+ ions, which influences diverse processes such as aggregation [33]. Radiolysis of organic solvents is more complex, and results in a mixture of solvated electrons, molecular hydrogen, organic radical species, and even large polymeric molecules [45].

2.2.5   Electron Beam Heating

A local temperature rise under electron irradiation is expected when the transferred energy is dissipated in the form of heat with or without damage. Heating is dominated by inelastic electron–electron scattering while the transferred energy in elastic electron–nucleus collisions is much lower.

Supposing the specimen is bounded by a circular heat conductor of infinite conductivity held at a fixed temperature and the irradiation intensity is symmetrical within the circle, the temperature in the specimen is determined by 2D heat conduction, and the maximum temperature rise is given approximately by [46]

$$\Delta T = \frac{I}{4\pi\kappa} \frac{\Delta E}{t} \left(\gamma + 2\ln\frac{R}{r} \right), \tag{2.6}$$

where R and r are the radii of the specimen and the beam, respectively, κ is the thermal conductivity of the specimen, γ is Euler's constant, and ΔE is the average energy loss in a specimen of thickness t. The average energy loss for relativistic electrons can be estimated by [46]

$$\frac{\Delta E}{t} = \frac{2\pi e^4 N Z}{m v^2} \left\{ \ln\left[\frac{E_0 (E_0 + m_e c^2)^2 \beta^2}{2 E_{ex}^2 m_e c^2} \right] + (1 - \beta^2) \right.$$
$$\left. - (1 - \sqrt{1 - \beta^2} + \beta^2)\ln 2 + \frac{1}{8}\left(1 - \sqrt{1 - \beta^2}\right)^2 \right\} \qquad (2.7)$$

where N is Loschmidt's number and E_{ex} is the excitation energy which is almost proportional to the atomic number Z. As a result, the temperature rise is independent of specimen thickness and proportional to the average density of the specimen. It can also be seen that the temperature rise is proportional to the beam current I and inversely proportional to the thermal conductivity. Generally, the temperature rise in TEM specimens during imaging is insignificant, provided the specimen is thin enough (order of magnitude 10 nm), as it is the case for typical lattice-resolution TEM studies. However, beam heating may be a serious problem at high incident currents, and it is detrimental for the specimen with quite low thermal conductivities.

Generally, heating is less if the electron energy is high, which seems quite counter-intuitive, but is due to the decreasing cross section for inelastic scattering towards higher energies. It is therefore preferable to use high acceleration voltages if the specimens are thermally unstable. However, possible damage by atom displacements has to be taken into account. On the other hand, good conductive contacts between specimen and support or specimen holder can enhance thermal dissipation, therefore reducing the beam-induced temperature rise of the specimen.

2.2.6   Electron Beam-Induced Deposition

Electron beam-induced deposition occurs when the irradiation is carried out in the presence of either volatile species in an atmosphere around the specimen or when mobile species are attached to the specimen surface. These species dissociated into volatile and nonvolatile components under the electron beam. The former disappears into the vacuum, while the latter adheres to the substrate, resulting in a local increase in thickness. Conversely, if the beam-activated molecules react with the specimen so that volatile species form, the substrate might be etched. Both deposition and etching occur only locally at or around the irradiated area.

In TEM, the most common deposition results from residual hydrocarbon, which is known as hydrocarbon contamination, especially in the STEM mode. Normally, hydrocarbon contamination is dominant around room temperature, whereas at high or low specimen temperatures it is negligible. At low specimen temperature, the mobility of hydrocarbon molecules on the specimen surface is too low to reach the

irradiated surface and, at high temperature, hydrocarbons evaporate from the specimen before being cracked by the electron beam. For hydrocarbon contamination, the precursors consist of the gaseous hydrocarbons in the vacuum (e.g., oil from the pumping system) and the adsorbed hydrocarbons on specimen surface (impurities by adhesion of molecules during specimen preparation or from the air). The deposition process is complex, consisting of specimen–hydrocarbon interaction, electron–specimen interaction, and electron–hydrocarbon interaction. The most important mechanism is governed by highly mobile hydrocarbon molecules that diffuse rapidly over the specimen surface. Once the molecules diffuse into the irradiated area, they are cracked so that immobile amorphous carbon is left on the specimen. Such a carbon deposit can be removed by plasma treatment, which is normally done *ex situ*. Intuitively, there are many factors involved in hydrocarbon contamination, such as beam current density, dissociation cross section, the residence time of hydrocarbons on specimen surface, specimen geometry, and the orientation of hydrocarbons with respect to the deposition location [47]. Some of the factors are almost impossible to control during the experiments, but it is certain that the diffusion of hydrocarbons along the specimen surface provides the major source because the contamination seriously occurs at the edge of the irradiated area as a ring in TEM imaging [48]. If the electron beam is focused onto spots with diameters smaller than several nanometers, a dot rather than a ring is formed. A line and even more complicated shapes can be formed by deflecting the beam.

Although this effect can be applied for lithography [49] and the fabrication of three-dimensional (3D) structures [50], it should generally be avoided for *in situ* experiments because the deposited layer might alter the behavior of the specimen [51]. Beam shower (short-time pre-illumination with a strong electron beam flux) is frequently employed to suppress hydrocarbon contamination. Heating may also reduce the hydrocarbon contamination rate by a factor of 10–30, depending on the temperature [52].

2.3 Electron Irradiation-Induced Processes in Nanomaterials

In situ electron irradiation experiments can be carried out in every standard TEM, even without technical modifications. Considering that the specimen temperature has a major influence on the evolution of radiation defects, a dedicated heating specimen stage is generally of advantage. On this basis, many irradiation phenomena in nanostructured materials were observed accidentally. This section presents some examples of electron irradiation-induced processes on the atomic scale in five main categories: (1) structural dynamics of defects, (2) phase transformations, (3) nucleation and growth of nanostructures, (4) generation and modification of novel structures, and (5) mechanical deformation.

2.3.1 The Dynamics of Defects Under Electron Beam Irradiation

The rise of 2D materials with atomic thickness such as graphene has opened a new window for the TEM observation of individual point defects such as vacancies or interstitials. As the atom positions in atomically thin 2D sheets can be intuitively identified from high-resolution image series, a detailed picture of the rearrangement of individual atoms under irradiation becomes visible without any imaging artifacts due to overlapping atoms or projection effects. Therefore, we focus on the electron irradiation-induced defect dynamics observed in 2D materials at the level of single atoms.

Typically, 2D materials are more sensitive to electron irradiation than 3D materials due to the fact that almost every atom is a surface atom. Displacement and ionization damage are the most relevant electron beam-induced processes. As shown in Table 2.2, the incident threshold electron energy for displacing C atoms in a graphene sheet is 86 keV at room temperature [12], which means that pristine graphene remains stable at a TEM voltage of 80 kV. But when contamination is adsorbed on the surface, atomic defects can be created at contamination sites in graphene even if the incident electron energy is much lower than the threshold energy [37]. As shown in Fig. 2.1a monovacancy forms at an adatom site under an 80 keV electron beam, which is attributed to a beam-induced chemical reaction of an adatom with the graphene substrate. Similarly, anion vacancies can be generated in pristine transition metal dichalcogenides (TMDC, such as MoS_2, $MoSe_2$, WS_2, etc.) sheets even if the incident electron energy is lower than the threshold energy for displacements [53], which probably results from the ionization effects.

The atomic defect continues growing so that holes are formed because atoms with unsaturated bonds around the vacancy are removed more easily than atoms within the sheet without dangling bonds [54]. In the case of graphene, Meyer et al. found that the growth of extended holes is not dominated by displacements because the growth rate of holes only weakly depends on the beam energy within a wide range of 20–100 keV [37]. Holes can form and grow in graphene even under a 20 keV electron beam, which is not expected from displacement effects because the threshold energy for displacing edge C atoms is assumed to be close to 50 keV. The observation that the growth rate of the holes is related to the vacuum level in the column further confirms that hole growth may be predominantly beam-induced etching by residual water or oxygen in the system [37]. It is worth noting that the shape of as-formed

Table 2.2 Displacement threshold energy E_d and corresponding energy of the beam electrons E_{thr} for typical 2D materials [12]

Materials	Graphene	h-BN		MoS_2		$MoSe_2$	WS_2
		B	N	S	Mo	Se	S
E_d (eV)	16	16	14	6.1	13.9	5.6	6.3
E_{thr} (keV)	86	74	84	83	430	175	86
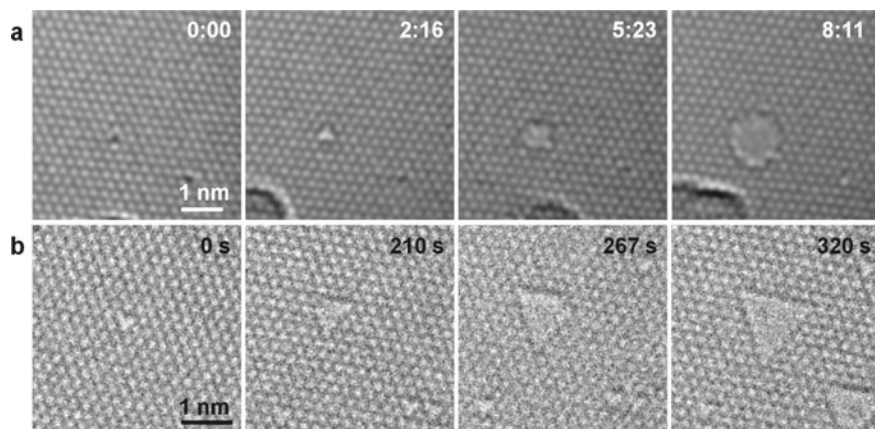
Fig. 2.1 Formation of holes starting from atomic defects under 80 keV electron beam irradiation. **a** Circular hole in graphene. Irradiation intensity is 700 A/cm^2. **b** Triangular-shaped hole in a monolayer of *h*-BN. Irradiation intensity is 480 A/cm^2

holes usually depends on the crystal structure of 2D substrate. As shown in Fig. 2.1, the monovacancy prefers to evolve into a circular hole in graphene; however, a triangular-shaped hole with N-terminated zigzag edges forms in monolayer *h*-BN at room temperature under 80 keV electron beam irradiation. Besides, the specimen temperature is expected to affect the shape of the hole. Rhomb-shaped and hexagonal holes with both B- and N-terminated edges become prominent in monolayer *h*-BN if the sheet is heated to above 700 °C during electron beam irradiation [55].

The atomic defects can also migrate over a long distance and agglomerate with other atomic defects under electron irradiation, resulting in the formation of more extended defects. It is obvious that defect migration is more frequently observed than their formation because the migration barrier is generally far less than the displacement threshold. Taking graphene as an example, prolonged electron beam irradiation will make isolated vacancies agglomerate into large multivacancies consisting of rotated hexagons and other polygons, but the multivacancies tend to reorganize into a dislocation dipole terminated by two-edge dislocations if the number of sputtered C-atoms is larger than 10 [56]. In the case of MoS_2, the diffusion of S-vacancies under the 80 keV electron beam is significantly fast and accelerated as the local vacancy concentration increases; therefore, S-vacancies are prone to agglomerate to form two typical straight-line defects [57]. It should be noted that the line defects do not only grow but also migrate occasionally under electron beam irradiation. In BN monolayers, Cretu et al. found that square-octagon line defects, involving less favorable B–B and N–N bonds, can migrate within monolayer *h*-BN at a temperature above 700°C through the glide of one or two atomic rows along the armchair direction [58].
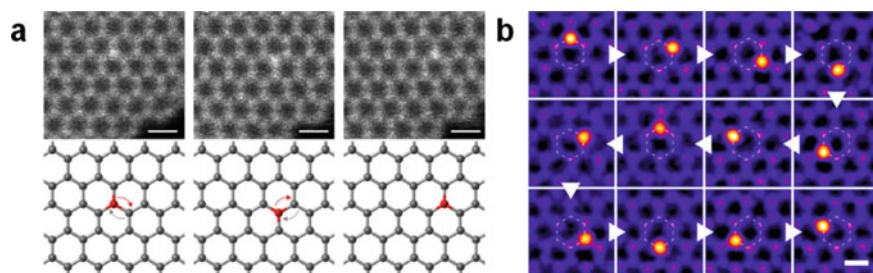
Fig. 2.2 Migration of foreign atoms in graphene under the electron beam. **a** Structural dynamics of a graphitic-N substitution via C–N bond inversion. Scale bar is 2.5 Å (reproduced with permission from Ref. [60], Copyright 2015, American Chemical Society). **b** Electron beam-controlled migration of Si substitution around a single hexagon. Scale bar is 2 Å (reproduced with permission from Ref. [32], Copyright 2018, American Chemical Society)

On the other hand, structural defects in 2D sheets can act as a trapping site for adatoms. However, the trapped atoms may still be mobile under electron beam irradiation. For example, Robertson et al. observed that Fe substitutions occupying a monovacancy or divacancy in graphene can move to adjacent lattice positions and reversibly switch their bonding between four and three nearest neighbors under the electron beam [59]. Other impurity atoms in graphene also show similar behavior under irradiation. Lin et al. found that pyridinic-N substitution can jump forth and back repeatedly between equivalent bonding sites across a monovacancy, while a graphitic-N substitution can migrate in the graphene plane via C–N bond inversions [60], as shown in Fig. 2.2a. Similarly, Si substitutions can also migrate via out-of-plane C–Si bond inversions [61], and Si trimer can rotate in a multivacancy [62]. Those movements can be well controlled by directing the electron beam onto the desired position which is possible with atomic precision. As shown in Fig. 2.2b, an Si atom can be precisely moved around a single hexagon by parking the electron beam on the C neighbor in the direction the Si should move [32].

In addition, electron beam-induced bond rotation can also lead to the formation, migration, and reconstruction of structural defects by keeping the atom number constant. A typical example is the formation and annihilation of a Stone–Wales (SW) defect in pristine graphene [63], as shown in Fig. 2.3a. An SW defect is considered to be formed by an in-plane 90º rotation of a C–C bond (SW rotation), and the kinetic barrier is 9–10 eV [64]. The maximum energy transferred from even 60 keV electrons is below the displacement threshold energy but sufficient to form multiple SW defects. Another typical example is the formation and annihilation of closed-loop "flower defects" [65]. Such a flower-like defect can be created via six consecutive bond rotations and relax into a less disordered state or even turn back to the pristine lattice by C–C bond rotations. Some other novel defects have also been created in 2D sheets through bond rotations. Lin et al. found a new threefold symmetric trefoil-like defect in monolayer TMDCs created via 60º rotations of metal–chalcogen bonds in the trigonal prismatic lattice [66]. The defect can expand through sequential

bond rotations and eventually evolve into larger linear defects consisting of aligned 8–5–5–8 membered rings.

Bond rotations can lead to structural transformations between several different configurations. As shown in Fig. 2.3b, the 5–8–5 (two pentagons separated by one octagon) divacancy can convert to a 5555–6–7777 defect (one hexagon surrounded by four pentagon–heptagon pairs) by means of a 555–777 (three circularly arranged pentagon–heptagon pairs) configuration [67], which releases the strain and reduces the influence of the divacancy onto the surrounding hexagonal lattice [68]. Bond rotation-mediated structural transformations also take place between various configurations of a tetravacancy [69]. Nevertheless, the most frequently observed tetravacancies are extended linear structures during the transformation, although they do not have the lowest formation energy. However, they are in a metastable state with
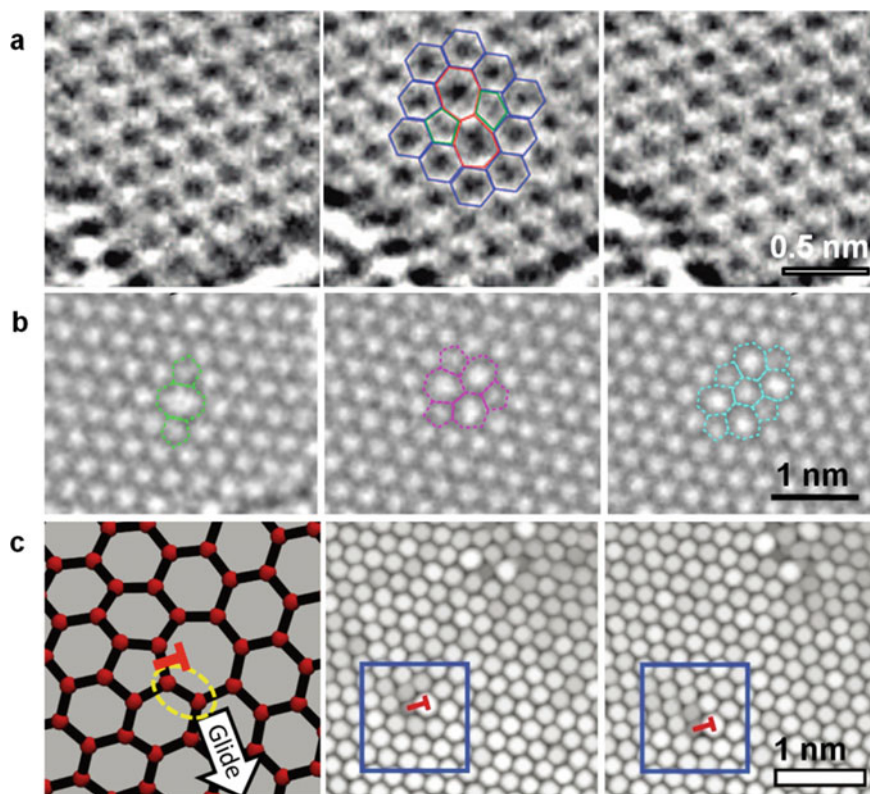
Fig. 2.3 Bond rotation-induced structural evolutions in graphene under 80 keV electron beam irradiation. **a** Formation and annihilation of a Stone–Wales defect (reproduced with permission from Ref. [63], Copyright 2008, American Chemical Society). **b** Transformation of a divacancy between different configurations (reproduced with permission from Ref. [67], Copyright 2011, American Physical Society). **c** Gliding of an edge dislocation via bond rotation (reproduced with permission from Ref. [56], Copyright 2013, Springer Nature)

a local energy minimum in the overall energy landscape. It is known that electron irradiation generally drives the system away from thermal equilibrium.

Bond rotations can also lead to the migration of structural defects, such as a random walk of divacancies [67] and dislocation glide in graphene [56]. As shown in Fig. 2.3c, the dislocation core consisting of a pentagon–heptagon pair can glide along the zigzag direction in graphene with a step of 0.25 nm via bond rotations [56]. Grain boundaries in 2D sheets can also migrate under electron beam irradiation. Kurasch et al. found that grain boundaries in graphene can migrate under electron beam irradiation via bond rotation, and the driving force depends only on the in-plane curvature of grain boundaries rather than on the detailed atomic arrangements [65]. The grain boundary with low curvature undergoes configuration changes without a preferred direction of migration. In contrast, the grain boundary with high curvature is expected to migrate towards the center of curvature, thereby shrinking the grain located on the same side of the boundary. The closed grain boundary can even unwind and restore towards the pristine lattice [65].

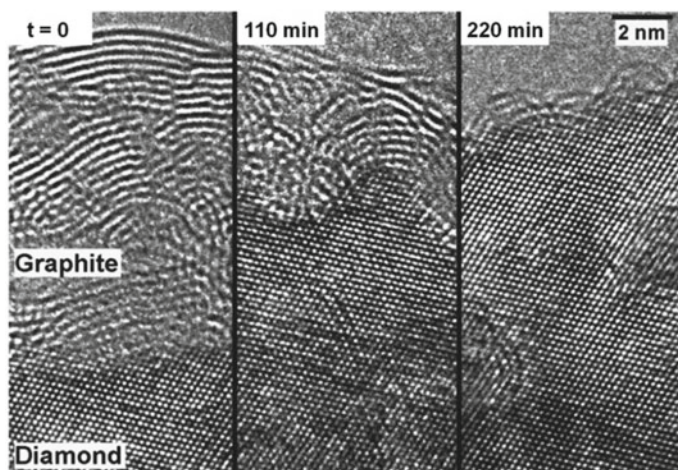### 2.3.2 Irradiation-Induced Phase Transformations

It is known for a long time that electron beam irradiation-induced structural changes can lead to phase transformations in the irradiated specimen area. Such transformations can be classified into two categories, namely (1) changes in morphology or crystal structure and (2) changes in composition.

Electron beam irradiation-induced changes in morphology or crystal structure have been observed in many different materials systems. An example is beam-induced complete disordering of a stable crystalline structure and transformation into a metastable amorphous phase. Conversely, the crystallization of metastable amorphous materials has also been observed frequently under the electron beam. In the case of carbon, electron irradiation can transform graphene sheets into a quasi-amorphous 2D membrane with a random arrangement of polygons when the incident beam energy is just above the threshold energy for displacements [67]. On the other hand, the graphitization of amorphous carbon can also be achieved by electron irradiation. Börrnert et al. found that freestanding amorphous carbon converted into graphitic carbon onions, while amorphous carbon supported on flat 2D sheets graphitized in a planar structure parallel to the support sheet due to van der Waals interactions with the underlying support [70]. With respect to the case of an amorphous carbon cluster on a 2D sheet, heat dissipation either through the underlying substrate or by radiative process is negligible, thus the cluster can potentially heat up significantly as the cluster volume decreases [70].

The transformation between different crystalline phases can also be achieved by electron irradiation. In carbon nanocrystals, for example, flat graphene flakes can curl up by sterical stress due to pentagonal rings which are introduced by electron beam-induced sputtering of edge C atoms, until it is able to zip up its open edges to form a completely closed fullerene [71]. Similarly, the formation of spherical onion-like

graphitic particles by electron irradiation of flat graphitic precursors is predictable [72]. When such carbon onions are exposed to sustained electron irradiation at high temperature, the gradual loss of C atoms from the surface induces a shrinkage and self-compression of the onions. This leads to high pressure in the interior of the particles [72]. The pressure in the center is hydrostatic and may reach values higher than 40 GPa [73], which may be far inside the stability regime of diamond. The extreme curvature of the innermost shells may trigger changes in the hybridization of C atoms from sp^2 to sp^3, leading eventually to the formation of a diamond crystal in the center. Conversely, the transformation of diamond nanoparticles into carbon onions is also feasible under irradiation. However, the transformation may depend on the initial size of the diamond particles. Hiraki et al. found that 5 nm diamond particles can change into onions by 300 keV electron beam irradiation, while 20 nm particles don't transform into carbon cages but to a graphite layer on the surface of the diamonds [74].

A real phase transformation in carbon can also occur under electron irradiation at high temperature. The transformation of graphite to diamond has been observed experimentally, which is surprising, given the fact that graphite is thermodynamically the more stable phase of carbon at low pressure [75]. As shown in Fig. 2.4, irradiation at high temperature leads to the growth of a diamond crystal at the interface between graphite and diamond [75]. When C atoms at the interface are displaced, they can aggregate to either of the two phases but the lifetime of the interfacial atoms is higher when they are bound in the diamond phase (diamond has a higher radiation hardness than graphite). It is known that atoms in graphite are easier to be displaced due to the lower mass density and van der Waals stacking with much space between the basal planes.


Fig. 2.4 Electron beam irradiation-induced transformation of graphite to diamond at a temperature of 700 °C and a beam current density of 100 A/cm^2 (reproduced with permission from Ref. [75], Copyright 1999, AIP Publishing)

Dynamic studies of phase transformation in transition metal chalcogenide under electron beam irradiation have also been shown by several groups. In Cu_2S, the transformation temperature is relatively close to room temperature and the Cu_2S nanocrystal can be heated above its phase-transition temperature by controlled electron irradiation. Zheng et al. directly observed the structural fluctuations between the low- and high-chalcocite phases of Cu_2S nanorods in the TEM [76], which provided insight into the understanding of microscopic pathways of structural fluctuations. Another example is the transformation of semi-conducing 2H-MoS_2 to metallic 1 T-MoS_2 via lattice-plane gliding which is triggered by electron irradiation [77]. As shown in Fig. 2.5, the transformation starts with the formation of the α-phase precursor with three or four constricted zigzag chains, followed by local strain-caused S-plane or Mo–S atoms gliding if two non-parallel α-phases are in contact. Consequently, a triangular nucleus of the 1 T phase forms and further expands via migration of a β-boundary [77]. Such a transformation only occurs in the irradiated region so that this can be easily controlled in STEM mode of the microscope.

Irradiation-induced changes in composition are also frequently observed in compounds consisting of two or more elements. It is natural that the element ratio will change if the rate of loss for different elements does not match the initial stoichiometry of the specimen. Consequently, the transformation between phases with different stoichiometry is feasible under irradiation [78–81]. Taking layered tin dichalcogenides as an example, the progressive removal of chalcogen atoms can be achieved by irradiation in a controllable manner, which first results in the formation of a mixed mono- and dichalcogenide and is followed by complete conversion to highly anisotropic orthorhombic monochalcogenides [82]. Figure 2.6a presents, as an example, the transformation from rhombohedral SnS_2 to highly anisotropic orthorhombic SnS. Another example is the transformation of bilayer $PdSe_2$ to monolayer Pd_2Se_3 by creating Se vacancies using electron irradiation [83]. The undercoordinated Pd atoms tend to bond with the nearest Se atoms in the adjacent layer, which creates a quantum force that pulls two layers towards each other. As the concentration of Se vacancies increases, the interlayer distance decreases to the length of a typical Pd–Se bond, resulting in the merging of the two layers and eventually the formation of the new Pd_2Se_3 2D phase [83]. Figure 2.6b presents the formation of monolayer Pd_2Se_3 which has a misoriented angle relative to the parent bilayer $PdSe_2$.

Eventually, some elements may be totally lost under the electron beam, resulting in the decomposition of the specimen [84]. For instance, under electron beam irradiation, the hexagonal $γ$-$CaSO_4$ will transform into a transient orthorhombic $β$-$CaSO_4$ and eventually CaO phase, accompanied with the complete loss of S element [85]. Another common example is the decomposition of radiation-sensitive crystals, e.g., organic–inorganic hybrid perovskites [86]. Chen et al. found that single-crystalline $CH_3NH_3PbI_3$ rapidly decomposes into hexagonal PbI_2 through the loss of iodine ions and subsequent collapse of the perovskite structure [86].

The change in composition as mentioned above is attributed to partial loss of components. Conversely, a phase transition by adding a new component to the specimen is feasible if both the specimen and the feedstock for new components are exposed together to electron bombardment. For instance, electron beam-induced
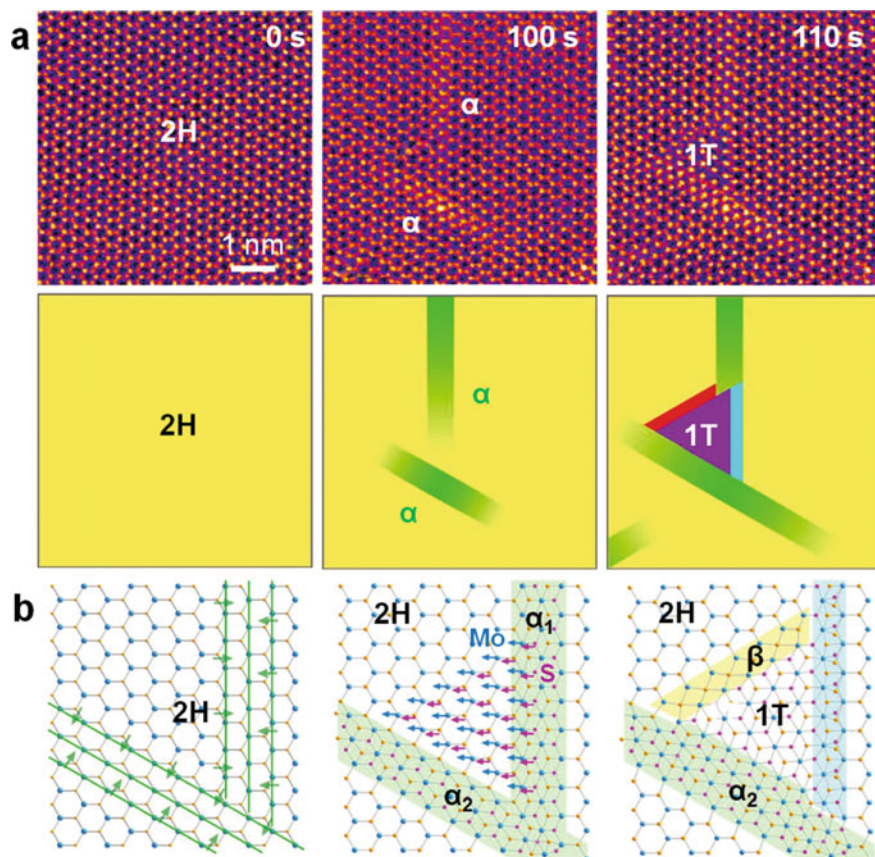
Fig. 2.5 Transformation between different crystalline phases in monolayer MoS_2 at 600 ℃ (reproduced with permission from Ref. [77], Copyright 2014, Springer Nature). **a** STEM image series and corresponding models showing the step-by-step progress of the phase transformation. **b** Model of atomic movements in the phase transformation

substitutional C doping can gradually transform *h*-BN sheets and tubes into hybrid ternary B–C–N honeycomb structures when a BN network with adsorbed hydrocarbon molecules is exposed to the electron beam [87]. It is understandable that B and N vacancies generated by electron irradiation are healed by C atoms that stem from decomposed hydrocarbon molecules. Another example is the formation of a metal carbide when graphitic onions encapsulating metals are subjected to electron irradiation in the TEM [88]. Such a transformation is induced by ballistic displacements of interface atoms and by the high pressure that the graphite shells exert onto the encapsulated metal particle.
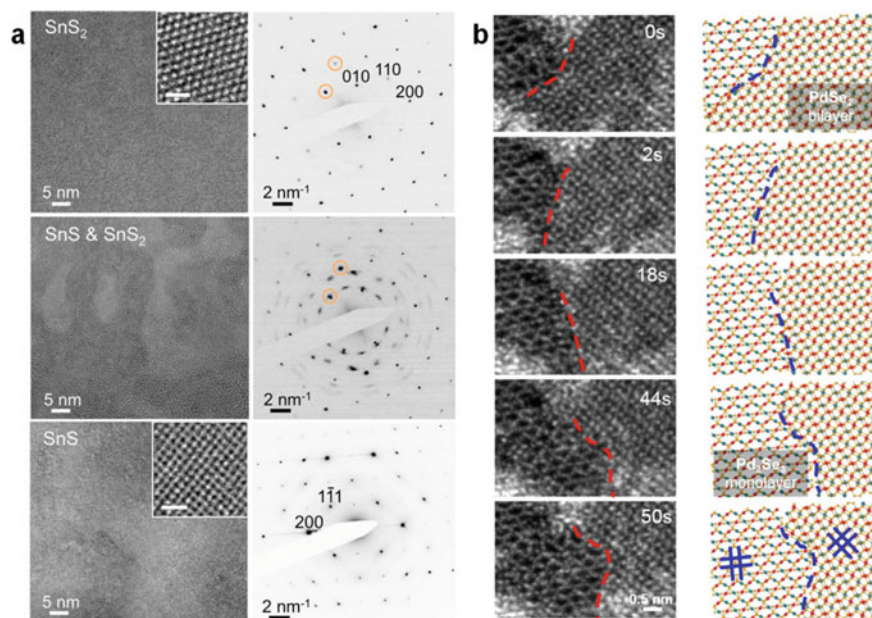
Fig. 2.6 Phase transformation between structures with different stoichiometry under electron irradiation. **a** The transformation from SnS_2 to SnS (reproduced with permission from Ref. [82], Copyright 2016, American Chemical Society). **b** The transformation from bilayer $PdSe_2$ to monolayer Pd_2Se_3 (reproduced with permission from Ref. [83], Copyright 2017, American Physical Society)

2.3.3 Nucleation and Growth of Nanostructures Under Irradiation

It has been shown that electron irradiation can trigger the nucleation and growth of nanostructures. Real-time observation of nucleation and growth has, for a long time, been carried out under vacuum condition in conventional TEMs, whereas new environmental specimen stages allow using gaseous and liquid precursors (see details in other chapters). Here, we focus on the nucleation and growth of nano-objects under vacuum conditions during which electron irradiation plays an essential role.

The key to study nucleation and growth inside a conventional TEM is to choose appropriate precursors which can be introduced into the specimen chamber and released in sufficient quantities to lead to the growth of the desired structures. Gas residues in the column and surface adsorbate on specimens or specimen grids are possible feedstocks, which provide small amounts of C and O atoms for growth. A simple experiment is the controlled growth of a metal oxide under electron beam irradiation. For instance, pure Ag can be locally oxidized as signified by the nucleation and growth of Ag_2O islands on its surface (Fig. 2.7) [89]. Interestingly, the Ag_2O structures only nucleate in the irradiated area under a low beam current density ($\sim 10^2$ A/cm^2). Although Ag is resistant to oxidation by molecular oxygen at room
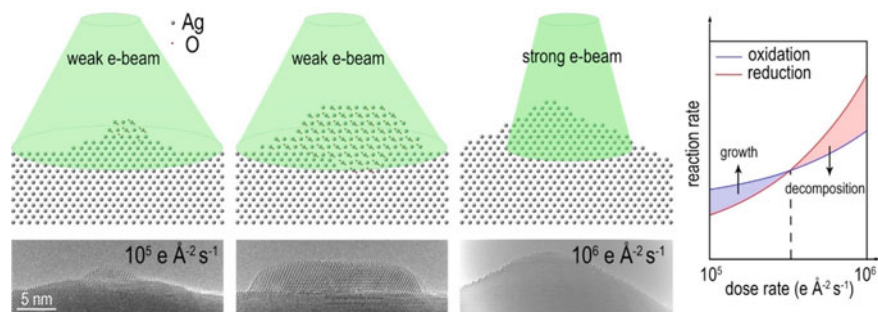
Fig. 2.7 Beam density-dependent nucleation and decomposition of the Ag_2O island on the Ag substrate (reproduced with permission from Ref. [89], Copyright 2019, Royal Society of Chemistry)

temperature, O_2 molecules adsorbed on the surface can be split into active radicals by electron irradiation and then react with the Ag substrate. It should be noticed that the Ag_2O islands can be fully reduced back to elemental Ag with an increase in the beam density (~10^3 A/cm^2). The controllable oxidation and reduction at different beam densities imply that electron beam may play a complex role in TEM studies of metal structures, especially when the metal is easily oxidized in air ambient, such as Mg [90, 91] or Fe [92]. Another example is the formation of In_2O_3 nanoparticles on the surface of In_2S_3 polycrystalline sheets [93]. The dangling bonds, resulting from electron beam-induced bond distortion, react with residual traces of O and water vapor in the TEM column, thus forming In_2O_3 nanoparticles.

For an efficient deposition, the precursor materials (substrates) should be highly unstable and easy to manipulate with the electron beam. When tiny amounts of an explosive precursor are irradiated by electron beam with sufficient beam density, the explosive decomposition happens due to heating or electrical charging. Consequently, a large number of nanoparticles are ejected outwards and caught by support membrane. Such a beam-induced fragmentation is mostly used for the production of metallic nanoparticles consisting of a single element [94].

If the precursor is decomposable under irradiation, the nucleation and growth may follow the beam-induced decomposition of the substrate and atomic rearrangements in the domain that is previously chemically modified. In many cases, amorphous films are used for the nucleation and growth of crystalline nanoparticles inside the amorphous matrix. For instance, crystalline Si nanoparticles can be formed within an amorphous SiO_2 film through either amorphous Si film [95] or amorphous $SiOx$ ($x < 2$) nanoparticles [96]. The substrates can also be polymers or metal–organic frameworks filled with the desired precursor [94]. At times, one-dimensional (1D) nanostructures can also grow with the help of a catalyst. Gonzalez-Martinez et al. demonstrated a straightforward route to grow amorphous core–shell B/BOx nanowires and BOx nanotubes by irradiating a composite made of Au nanoparticles embedded within an amorphous BOx matrix [97]. The Au nanoparticles were initially guided toward the composite surface by the condensed electron beam and then catalyzed the growth of a 1D structure in the presence of oxygen species. The B^+ ions generated within
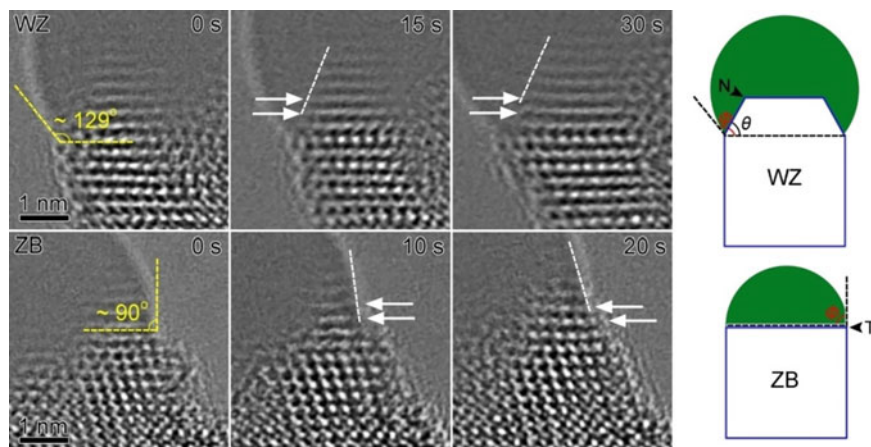
Fig. 2.8 The growth kinetics of wurtzite and zinc blende ZnO nanowires under 200 keV electron beam (reproduced with permission from Ref. [98], Copyright 2018, American Chemical Society)

the irradiated volume through charging and a Knotek–Feibelman mechanism could diffuse to the reaction sites in the Au nanoparticles due to electrostatic repulsion. The growth of coaxial B/BOx nanowires continued as long as enough B species were supplied, and the catalytic process could use B from the core of a coaxial nanowire, forming eventually a BOx nanotube if the quantity of the B species was insufficient [97]. Another example is Sn-catalyzed growth of ZnO nanowires by electron beam irradiation of Zn_2SnO_4 (Fig. 2.8) [98]. Sn became liquid droplet under electron irradiation due to low melting point (~505 K), and diffused onto the surface of Zn_2SnO_4, catalyzing the growth of wurtzite or zinc blende nanowires. Even without a catalyst, 1D structures can grow rooted at their base to the precursor materials and be extruded by a beam-induced field gradient within the substrates [99].

If the precursor is easily damaged, nucleation and growth phenomena are frequently observed. An example is the growth of a carbon nanotube from a metal (e.g., Fe, Co, Ni, or Fe/Co alloy) encapsulated partially by a host nanotube when subjected to electron beam irradiation at high temperature [100], as shown in Fig. 2.9. Carbon atoms from the shells are ejected into the encapsulated FeCo crystal and precipitate at the uncovered metal as an extended array of C filaments after a short time, because the solubility of C in these metals is low but the diffusion is fast. Ordering of the filament eventually leads to the growth of another carbon nanotube inside the host tube. In such an experiment, the host carbon nanotube is utilized both as a feedstock material and as a local template.

Another example is the aggregation and rearrangement of beam-introduced adatoms on the surface or at the defect sites, which manifests itself as epitaxial growth or healing [101–103]. As mentioned above, most displaced atoms at the surface are weakly bonded and able to diffuse over the surface under the electron
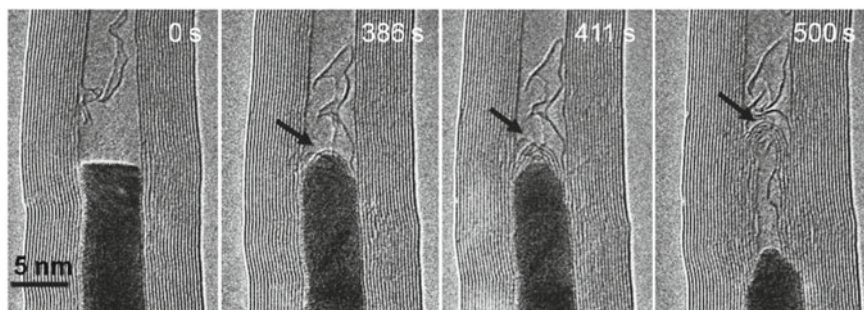
Fig. 2.9 Growth of a new nanotube from a FeCo crystal inside the host carbon nanotube. Temperature is 600 °C and irradiation density is 100 A/cm^2 (reproduced with permission from Ref. [100], Copyright 2007, Springer Nature)

beam, which provides the source for epitaxial growth or annealing. This has been observed for the healing of holes in MoS_2 and Bi_2Te_3 and is shown in Fig. 2.10 [103].

2D structures may also form from clusters if the transferred energy is sufficient to trigger the reconstruction. Zhao et al. found that Fe residues were able to entirely fill small perforations in graphene and thus form free-standing crystalline single-atom Fe layers [104]. The lattice constant for such Fe membranes was larger than bulk Fe and increased towards the center of the membranes due to the strain resulting from the lattice mismatch between graphene and the suspended Fe sheet. However, the largest stable Fe monolayer is only 10–12 atoms wide [104]. Similarly, metal oxide monolayers can form both on graphene substrates and inside graphene nanopores. This has been observed for crystalline single-atom CuO membranes on graphene substrates and is shown in Fig. 2.11 [105].
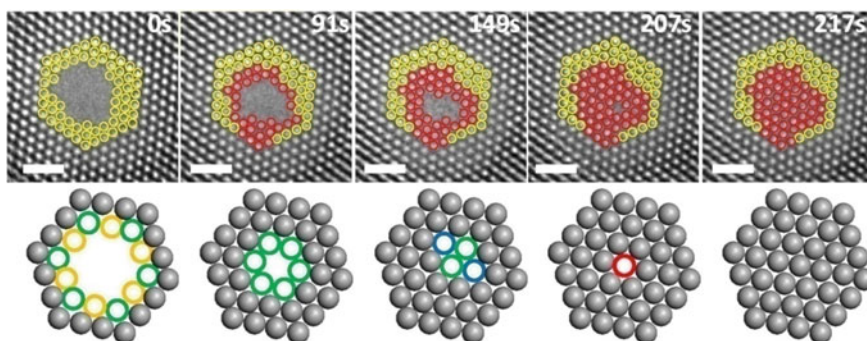
Fig. 2.10 Healing of a nanohole in Bi_2Te_3 under a 300 keV electron beam. Irradiation density is 16 A/cm^2, scale bar is 1 nm (reproduced with permission from Ref. [103], Copyright 2018, John Wiley and Sons)
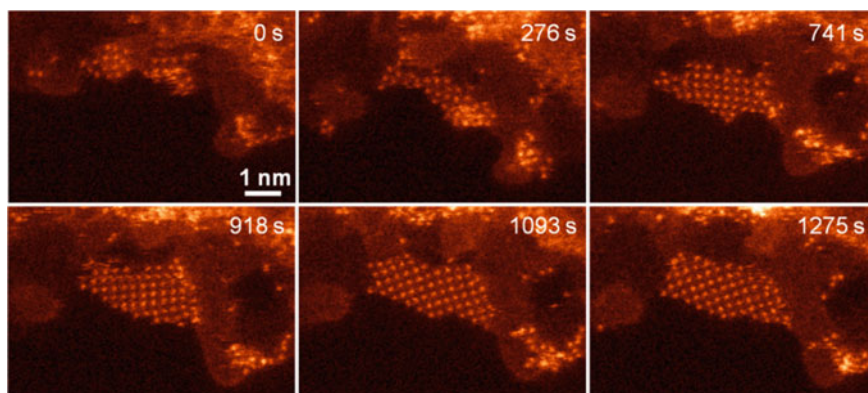
Fig. 2.11 Growth of a CuO membrane of monoatomic thickness on a graphene substrate (reproduced with permission from Ref. [105], Copyright 2017, IOP Publishing)

2.3.4   Fabrication of New Structures Under Irradiation

Although the fabrication of nanodevices via electron irradiation inside an electron microscope remains a challenge due to the lack of operational flexibility, the creation of new structures with atomic precision as building blocks for devices is nevertheless of interest. Sub-nanometer 1D structures are among the most promising building blocks for future electronic devices. Hence, we focus on the fabrication of ultrathin 1D structures, such as atomic chains, nanowires, and nanotubes in this section.

A large number of experimental studies have shown that electron irradiation provides a top-down strategy to fabricate novel structures [106–111]. Normally, ultrathin quasi-1D structures can be created when holes are first drilled in thin films using a focused electron beam so that the size of the hole is given by the dimensions of the beam profile. A low-dimensional ribbon spans between two adjacent holes so that the initial size of the ribbons depends on the irradiated regions. Subsequently, extremely narrow ribbons and even atomic chains eventually form after further thinning.

As early as the late 1990s, Kondo et al. proposed that stable Au nanowires could be prepared by electron beam irradiation in a 3 nm-thick Au film through the formation of Au bridges between two neighboring holes and further thinning of the Au bridge [112]. The as-formed nanowires were 0.8 ~3 nm in diameter but remained stable due to surface reconstruction, leading to a hexagonal prism consisting of a hexagonal-close-packed surface layer and a face-centered-cubic core [112] or a coaxial tube with helical atom rows coiled round its axis [113]. Soon afterwards, Ugarte et al. reported that such an experimental procedure can be extended to atomic Au chains [114] and other ultrathin metal nanowires [115–117].

In the late 2000s, the technique was applied to sculpt natural 2D planes. As shown in Fig. 2.12a, linear C chains were made by further removing edge atoms from graphene ribbons [118]. Interestingly, the arrangement of C bonds in the chain seems to be affected by temperature and local strain. The as-formed 1D structure is

interpreted as a polyyne chain with alternating single and triple bonds if it is under strain, and a cumulene chain with uniform double bonds if it is unstrained [119]. These two distinct arrangements coexist at low or ambient temperature, while an unexpectedly high polyene ratio is observed in carbon chains fabricated at elevated temperatures [120]. Such a top-down method is also suitable for other 2D systems. Atomic chains with alternating B and N atoms have been created in h-BN sheets [121]; phosphorus chains with zigzag configurations have been created in phosphorene and their stability is enhanced if the chains are supported by a substrate [122].

Unlike atomic chains formed in graphene, h-BN, or phosphorene, extremely narrow wires can be constructed from TMDCs. As shown in Fig. 2.12b, ultra-narrow wires can be derived from monolayer MoS_2 by further thinning the ribbons between two adjacent holes [123]. Interestingly, the wire is robust under electron irradiation and its atomic structure is obviously different from the initial MoS_2. Similar structures can be created in other TMDC sheets, and the as-formed wires have been experimentally proven to be metallic [124]. On this basis, complex junctions of nanowires can form from narrow constrictions, and alloyed nanowires such as MoS_xSe_{1-x} can be fabricated by sculpting their alloyed monolayer counterpart or corresponding van der Waals heterostructures [125].

Similarly, bilayer nanoribbons can form between two adjacent pores in bilayer sheets. Sometimes, the dangling bonds at the edges can be saturated with interlayer
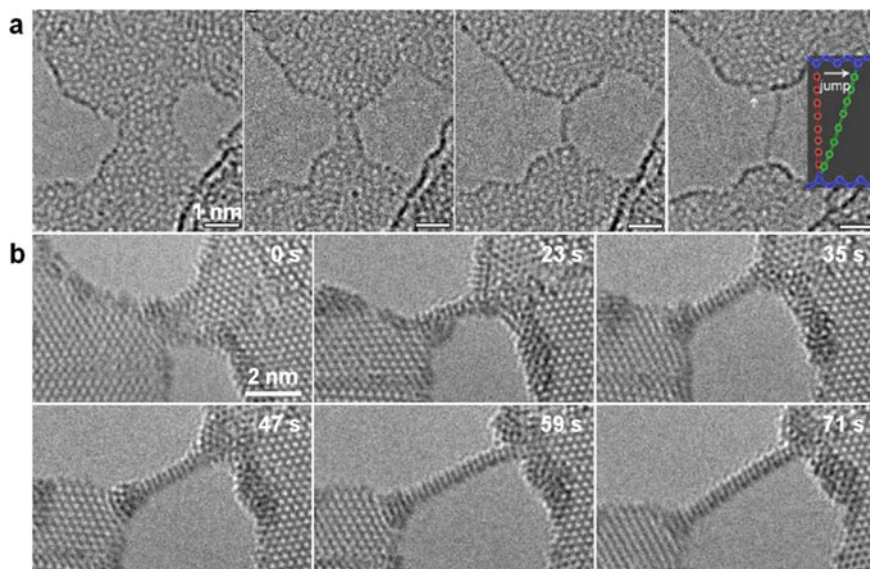
Fig. 2.12 Atomic wires sculpted from 2D sheets. **a** Formation of a free-standing C chain in graphene under a 120 keV electron beam. Irradiation intensity is 4 A/cm^2 (reproduced with permission from Ref. [118], Copyright 2009, American Physical Society). **b** Formation of a suspended wire in a MoS_2 sheet under an 80 keV electron beam. Irradiation intensity is 10 A/cm^2 (reproduced with permission from Ref. [123], Copyright 2013, Springer Nature)

bonds, resulting in a structural transformation from bilayer ribbons with open edges to single-walled tubular structures. For example, single-walled tubular structures can be fabricated in AA' stacked bilayer *h*-BN at predefined positions by controlling the location of pores, and then thinned by removing atomic rows one by one under sustained irradiation [126].

2.3.5 Deformation of Nanostructures Under Electron Irradiation

As pointed out above, intense electron irradiation can cause the shrinkage of graphitic shells when spherical carbon onions or cylindrical nanotubes encapsulating other crystals are subjected to electron bombardment at high temperatures. The self-contraction of the outer shells, which is due to the reconstruction of vacancies in the shells after the sputtering-induced loss of carbon atoms, can exert an enormous pressure on the encapsulated crystals, resulting in heavy deformation or extrusion effects. Generally, these experiments need a defined strategy to study in situ the deformation of individual nanometer-sized crystals at the atomic scale.

It is known that the polyhedral graphitic particles synthesized by arc discharge generally transform into a perfectly spherical "onion" under the electron beam. The process is facilitated at specimen temperatures above 300–400ºC where the graphitic shells reconstruct after the creation of radiation defects. During the morphological transformation, the encapsulated crystal is subjected to compressive forces and eventually deformation which manifests itself, besides visible shape changes, in a decrease in lattice spacing [73], or the formation of twins or grain boundaries [127]. The process is accessible to direct observation at atomic resolution. This has been observed for W and Mo crystals inside graphitic shells and is shown in Fig. 2.13a [127]. It should be noted that the crystals inside the onions have no freedom to evade the pressure (if the shells are closed); ultimately the atoms of the crystal may gradually diffuse through the graphite shells towards the surface [128]. If the shells have an opening, the crystal is squeezed out through the opening where particularly high stress appears to prevail [127]. Carbon onions that have been punctured with a focus electron beam allow to use them as extrusion cells to study the deformation of nanocrystals in detail under continuous load [129]. The plastic deformation of individual Au, Pt, Mo, and W crystals has been observed inside carbon onions which is shown in Fig. 2.13b [129]. Similarly, controlled irradiation of carbon nanotubes can cause large pressure buildup to the order of 40 GPa within the nanotubes. Therefore, carbon nanotubes can be used as robust jigs for deforming and extruding even hard materials such as iron carbide along the tube axis as shown in Fig. 2.13c [130].

In addition, as mentioned above, a large number of studies have demonstrated that electron irradiation provides a top-down strategy to fabricate nanowires. Interestingly, the as-formed nanowires have a tendency to elongate and even break under the electron beam mainly due to the existence of tensile strain, which results from the
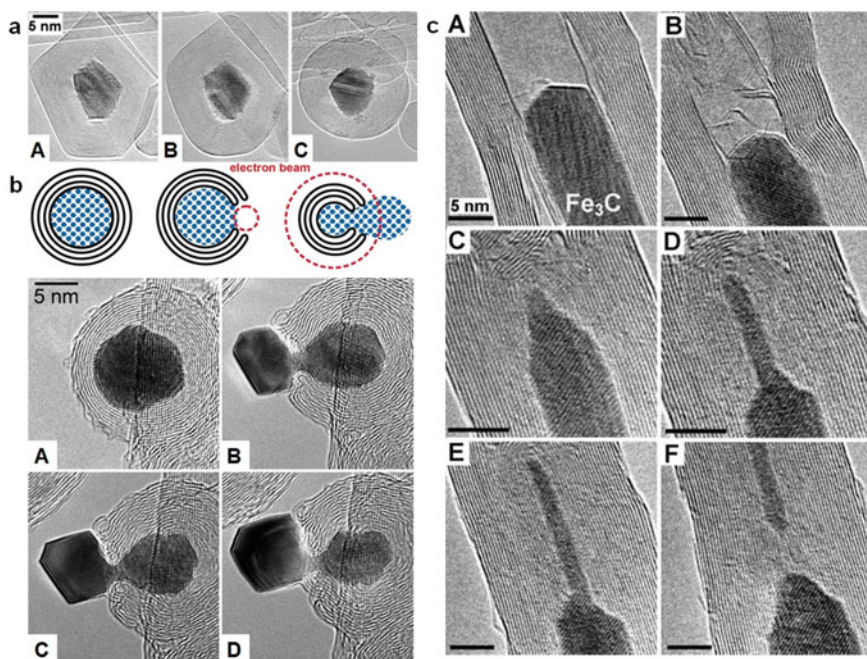
Fig. 2.13 Deformation of nanocrystals encapsulated inside graphitic shells under electron irradiation. **a** Deformation of a Mo crystal inside a carbon onion at 600 °C (reproduced with permission from Ref. [127], Copyright 2005, John Wiley and Sons). **b** Extrusion of an Au crystal from punctured onion at 300 °C (reproduced with permission from Ref. [129], Copyright 2008, American Physical Society). **c** Extrusion of a Fe$_3$C crystal inside a collapsing carbon nanotube along the tube axis at 600 °C (reproduced with permission from Ref. [130], Copyright 2006, AAAS)

relative displacement and/or rotation of the nanowire apexes, probably due to thermal deformation of the whole substrate. These experiments thus provide a method for the *in situ* study of structural changes under tensile strain. Several phenomena have been observed. Lagos et al. reported the spontaneous formation of the smallest possible hollow metal wires with a square cross-section during the elongation of Ag junctions and interpreted this configuration as a minimization of surface energy and generation of a soft structure, capable of absorbing a huge tensile deformation when high stress is applied [131]. Strain-mediated reversible phase transformations from the wurtzite structure to an intermediate body-centered tetragonal and *h*-MgO structure in quantum-confined ZnO nanowires (with a diameter less than 2 nm) have been observed using a similar approach (Fig. 2.14) [132]. Both *in situ* observation and theoretical calculations demonstrate that tensile stress plays a pivotal role in mediating the phase transformation.
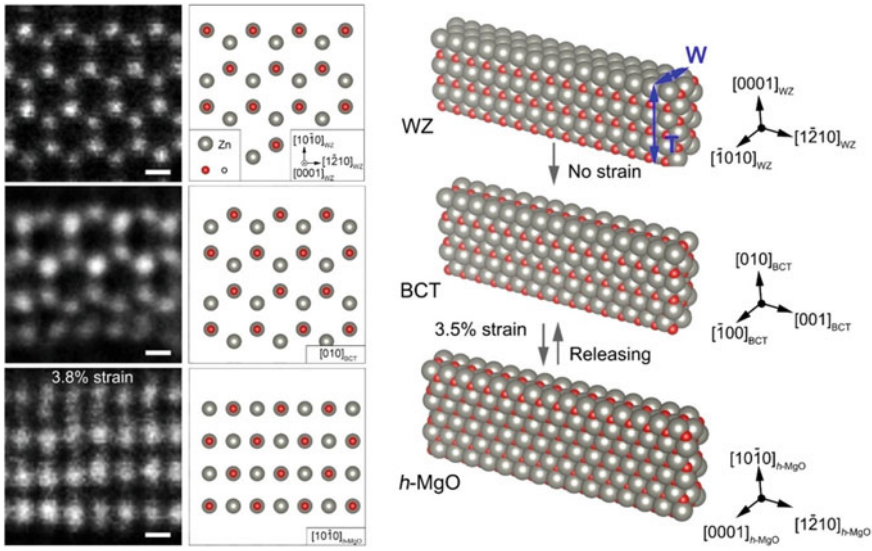
Fig. 2.14 The reversible phase transformation of a sub-2-nm ZnO nanowire. Scale bar is 2 Å (reproduced with permission from Ref. [132], Copyright 2019, American Physical Society)

2.4 Conclusions and Outlook

Although radiation damage is normally an unwelcome artifact, the electron beam can be intentionally used to trigger structural evolutions in a controllable way, while the structural changes can be monitored at the same time with the same beam. The ability to both generate and investigate structural transformations simultaneously made it possible that electron irradiation became an important direction of *in situ* microscopy.

In situ irradiation of nanomaterials has shown many phenomena of fundamental importance. Beam-induced structural transformations serve as models to understand the dynamic behavior of nanocrystals at the atomic scale and even the migration of individual atoms. The formation of secondary phases by electron irradiation, especially non-equilibrium phases, is expected to become a key experiment to develop and understand new nanostructured materials. However, there are still many technical challenges and opportunities, especially in the observation of dynamic phenomena at the atomic scale in beam-sensitive materials. Normally, the live observation requires instantaneous exposure of the material to the beam; however, the maximum electron dose for most beam-sensitive materials is low, which restricts the image resolution due to the poor signal-to-noise ratio at short exposure times. Some technological and methodological strategies, such as an electron detector coupled with direct-detection and electron counting techniques, low-dose imaging through compressive sensing, or pulsed laser-triggered ultrafast electron microscopy, have been proposed to improve

and extend the imaging capabilities [133], which is expected to expand our knowledge on radiation phenomena in beam-sensitive materials in the future. Besides, irradiation of composite systems may give the opportunity to study the response of one component to the stimulation arised from the radiation-induced evolution of the other component.

References

1. Xu T, Sun L (2015) Dynamic In-Situ experimentation on nanomaterials at the atomic scale. Small 11(27):3247–3262. https://doi.org/10.1002/smll.201403236
2. Egerton RF, Li P, Malac M (2004) Radiation damage in the TEM and SEM. Micron 35(6):399–409. https://doi.org/10.1016/j.micron.2004.02.003
3. Lembke A, Ruska H (1940) Vergleichende Mikroskopische und Übermikroskopische Beobachtungen un den Erregern der Tuberkulose. J Mol Med 19(10):217–220
4. Sheng H, Zheng H, Cao F, Wu S, Li L, Liu C, Zhao D, Wang J (2015) Anelasticity of twinned CuO nanowires. Nano Res 8(11):3687–3693. https://doi.org/10.1007/s12274-015-0868-x
5. Zheng H, Liu Y, Mao SX, Wang J, Huang JY (2012) Beam-assisted large elongation of in situ formed Li_2O nanowires. Sci Rep 2(1):542. https://doi.org/10.1038/srep00542
6. Sun J, He L, Lo Y-C, Xu T, Bi H, Sun L, Zhang Z, Mao SX, Li J (2014) Liquid-like pseudoelasticity of sub-10-nm crystalline silver particles. Nat Mater 13(11):1007–1012. https://doi.org/10.1038/nmat4105
7. Silk ECH, Barnes RS (1959) Examination of fission fragment tracks with an electron microscope. Phil Mag 4(44):970–972. https://doi.org/10.1080/14786435908238273
8. Cowley J (1966) Irradiation effects in beryllia and zinc oxide. Acta Crystallogr A 21(2):192–196. https://doi.org/10.1107/S0365110X66002603
9. Makin M (1968) Electron displacement damage in copper and aluminium in a high voltage electron microscope. Phil Mag 18(153):637–653. https://doi.org/10.1080/14786436808227466
10. Bursill L, Thomas J, Rao K-J (1981) Stability of zeolites under electron irradiation and imaging of heavy cations in silicates. Nature 289(5794):157–158. https://doi.org/10.1038/289157a0
11. Sun L, Banhart F, Warner J (2015) Two-dimensional materials under electron irradiation. MRS Bull 40(01):29–37. https://doi.org/10.1557/mrs.2014.303
12. Xu T, Yin K, Sun L (2017) In-situ study of electron irradiation on two-dimensional layered materials. Chin Sci Bull 62(25):2919–2930. https://doi.org/10.1360/N972016-01031
13. Xu T, Shen Y, Yin K, Sun L (2019) Precisely monitoring and tailoring 2D nanostructures at the atomic scale. APL Mater 7(5):050901. https://doi.org/10.1063/1.5096584
14. Stenn K, Bahr GF (1970) Specimen damage caused by the beam of the transmission electron microscope, a correlative reconsideration. J Ultrastruct Res 31(5):526–550. https://doi.org/10.1016/S0022-5320(70)90167-X
15. Thomas L, Humphreys C, Duff W, Grubb D (1970) Radiation damage of polymers in the million volt electron microscope. Radiat Eff 3(1):89–91. https://doi.org/10.1080/00337577008235620
16. Hobbs LW (1987) Electron-beam sensitivity in inorganic specimens. Ultramicroscopy 23(3):339–344. https://doi.org/10.1016/0304-3991(87)90244-0
17. Urban K (1979) Radiation-induced processes in experiments carried out in-situ in the high-voltage electron microscope. Phys Status Solidi A 56(1):157–168. https://doi.org/10.1002/pssa.2210560116
18. Burton E, Sennett R, Ellis S (1947) Specimen changes due to electron bombardment in the electron microscope. Nature 160(4069):565–567. https://doi.org/10.1038/160565b0

19. Hamm FA, Norman EV (1948) Transformations in Organic Pigments. J Appl Phys 19(12):1097–1109. https://doi.org/10.1063/1.1715026
20. Fischer RB (1954) Decompositions of Inorganic Specimens During Observation in the Electron Microscope. J Appl Phys 25(7):894–896. https://doi.org/10.1063/1.1721764
21. Hillier J, Mudd S, Smith AG, Beutner EH (1950) The "Fixation" of electron microscopic specimens by the electron beam. J Bacteriol 60(5):641–654
22. Wilkes P (1979) Phase stability under irradiation—a review of theory and experiment. J Nucl Mater 83(1):166–175. https://doi.org/10.1016/0022-3115(79)90602-0
23. Saka H, Noda K, Matsumoto K, Imura T (1975) Effect of electron irradiation on dislocation behavior in Ni during in-situ deformation experiment in HVEM. Scr Metall 9(5):499–504. https://doi.org/10.1016/0036-9748(75)90340-3
24. Cherns D, Hutchison JL, Jenkins ML, Hirsch PB, White S (1980) Electron irradiation induced vitrification at dislocations in quartz. Nature 287(5780):314–316. https://doi.org/10.1038/287314a0
25. Fisher SB, Williams KR (1972) Irradiation enhanced precipitation in stainless steel. Phil Mag 25(2):371–380. https://doi.org/10.1080/14786437208226811
26. Yagi K, Honjo G (1964) Transmission electron microscopy of sodium chloride films prepared by electron beam flashing thinning technique. J Phys Soc Jpn 19(10):1892–1905. https://doi.org/10.1143/jpsj.19.1892
27. Matsui S, Ichihashi T (1988) In situ observation on electron-beam-induced chemical vapor deposition by transmission electron microscopy. Appl Phys Lett 53(10):842–844. https://doi.org/10.1063/1.100089
28. Golberg D, Bando Y, Stéphan O, Kurashima K (1998) Octahedral boron nitride fullerenes formed by electron beam irradiation. Appl Phys Lett 73(17):2441–2443. https://doi.org/10.1063/1.122475
29. Furuya K (2008) Nanofabrication by advanced electron microscopy using intense and focused beam. Sci Technol Adv Mater 9(1):014110. https://doi.org/10.1088/1468-6996/9/1/014110
30. Krasheninnikov AV, Nordlund K (2010) Ion and electron irradiation-induced effects in nanostructured materials. J Appl Phys 107(7):071301. https://doi.org/10.1063/1.3318261
31. Banhart F, Ajayan PM (1996) Carbon onions as nanoscopic pressure cells for diamond formation. Nature 382(6590):433–435. https://doi.org/10.1038/382433a0
32. Tripathi M, Mittelberger A, Pike NA, Mangler C, Meyer JC, Verstraete MJ, Kotakoski J, Susi T (2018) Electron-Beam manipulation of silicon dopants in graphene. Nano Lett 18(8):5319–5323. https://doi.org/10.1021/acs.nanolett.8b02406
33. Schneider NM, Norton MM, Mendel BJ, Grogan JM, Ross FM, Bau HH (2014) Electron–water interactions and implications for liquid cell electron microscopy. The Journal of Physical Chemistry C 118(38):22373–22382. https://doi.org/10.1021/jp507400n
34. Williams DB, Carter CB (2009) Transmission Electron Microscopy, 2nd edn. Springer, New York
35. Banhart F (1999) Irradiation effects in carbon nanostructures. Rep Prog Phys 62(8):1181–1221. https://doi.org/10.1088/0034-4885/62/8/201
36. McKinley WA, Feshbach H (1948) The Coulomb scattering of relativistic electrons by nuclei. Phys Rev 74(12):1759. https://doi.org/10.1103/PhysRev.74.1759
37. Meyer JC, Eder F, Kurasch S, Skakalova V, Kotakoski J, Park HJ, Roth S, Chuvilin A, Eyhusen S, Benner G, Krasheninnikov AV, Kaiser U (2012) Accurate measurement of electron beam induced displacement cross sections for single-layer graphene. Phys Rev Lett 108(19):196102. https://doi.org/10.1103/PhysRevLett.108.196102
38. Egerton RF, McLeod R, Wang F, Malac M (2010) Basic questions related to electron-induced sputtering in the TEM. Ultramicroscopy 110(8):991–997. https://doi.org/10.1016/j.ultramic.2009.11.003
39. Egerton RF (2013) Beam-Induced motion of adatoms in the transmission electron microscope. Microsc Microanal 19(02):479–486. https://doi.org/10.1017/S1431927612014274
40. Cazaux J (1995) Correlations between ionization radiation damage and charging effects in transmission electron microscopy. Ultramicroscopy 60(3):411–425. https://doi.org/10.1016/0304-3991(95)00077-1

41. Hobbs LW (1990) Murphy's law and the uncertainty of electron probes. Scanning Microsc Suppl 4:171–183

42. McCartney MR, Crozier PA, Weiss JK, Smith DJ (1991) Electron-beam-induced reactions at transition-metal oxide surfaces. Vacuum 42(4):301–308. https://doi.org/10.1016/0042-207 X(91)90042-H

43. Henderson R, Glaeser RM (1985) Quantitative analysis of image contrast in electron micrographs of beam-sensitive crystals. Ultramicroscopy 16(2):139–150. https://doi.org/10.1016/ 0304-3991(85)90069-5

44. Isaacson M, Johnson D, Crewe A (1973) Electron beam excitation and damage of biological molecules; its implications for specimen damage in electron microscopy. Radiat Res 55(2):205–224. https://doi.org/10.2307/3573678

45. Woehl T, Abellan P (2017) Defining the radiation chemistry during liquid cell electron microscopy to enable visualization of nanomaterial growth and degradation dynamics. J Microsc 265(2):135–147. https://doi.org/10.1111/jmi.12508

46. Fisher S (1970) On the temperature rise in electron irradiated foils. Radiat Eff 5(2):239–243. https://doi.org/10.1080/00337577008235027

47. van Dorp WF, Hagen CW (2008) A critical literature review of focused electron beam induced deposition. J Appl Phys 104(8):081301. https://doi.org/10.1063/1.2977587

48. Xu T, Xie X, Yin K, Sun J, He L, Sun L (2014) Controllable atomic-scale sculpting and deposition of carbon nanostructures on graphene. Small 10(9):1724–1728. https://doi.org/10. 1002/smll.201303377

49. Meyer JC, Girit CO, Crommie MF, Zettl A (2008) Hydrocarbon lithography on graphene membranes. Appl Phys Lett 92(12):123110–123113. https://doi.org/10.1063/1.2901147

50. He L, Xu T, Sun J, Yin K, Xie X, Ding L, Xiu H, Sun L (2012) Investment casting of carbon tubular structures. Carbon 50(8):2845–2852. https://doi.org/10.1016/j.carbon.2012.02.051

51. He L-B, Zhang L, Tan X-D, Tang L-P, Xu T, Zhou Y-L, Ren Z-Y, Wang Y, Teng C-Y, Sun L-T, Nie J-F (2017) Surface energy and surface stability of ag nanocrystals at elevated temperatures and their dominance in sublimation-induced shape evolution. Small 13(27):1700743. https:// doi.org/10.1002/smll.201700743

52. Pashley DW, Stowell MJ, Jacobs MH, Law TJ (1964) The growth and structure of gold and silver deposits formed by evaporation inside an electron microscope. Phil Mag 10(103):127–158. https://doi.org/10.1080/14786436408224212

53. Komsa H-P, Kotakoski J, Kurasch S, Lehtinen O, Kaiser U, Krasheninnikov AV (2012) Two-dimensional transition metal dichalcogenides under electron irradiation: defect production and doping. Phys Rev Lett 109(3):035503. https://doi.org/10.1103/PhysRevLett.109.035503

54. Russo CJ, Golovchenko JA (2012) Atom-by-atom nucleation and growth of graphene nanopores. Proc Natl Acad Sci USA 109(16):5953–5957. https://doi.org/10.1073/pnas.111 9827109

55. Pham T, Gibb AL, Li Z, Gilbert SM, Song C, Louie SG, Zettl A (2016) Formation and dynamics of electron-irradiation-induced defects in hexagonal boron nitride at elevated temperatures. Nano Lett 16(11):7142–7147. https://doi.org/10.1021/acs.nanolett.6b03442

56. Lehtinen O, Kurasch S, Krasheninnikov AV, Kaiser U (2013) Atomic scale study of the life cycle of a dislocation in graphene from birth to annihilation. Nat Commun 4:2098. https:// doi.org/10.1038/ncomms3098

57. Komsa H-P, Kurasch S, Lehtinen O, Kaiser U, Krasheninnikov AV (2013) From point to extended defects in two-dimensional MoS$_2$: Evolution of atomic structure under electron irradiation. Phys Rev B 88(3):035301. https://doi.org/10.1103/PhysRevB.88.035301

58. Cretu O, Lin Y-C, Suenaga K (2014) Evidence for active atomic defects in monolayer hexagonal boron nitride–a new mechanism of plasticity in 2D materials. Nano Lett 14(2):1064–1068. https://doi.org/10.1021/nl404735w

59. Robertson AW, Montanari B, He K, Kim J, Allen CS, Wu YA, Olivier J, Neethling J, Harrison N, Kirkland AI, Warner JH (2013) Dynamics of single fe atoms in graphene vacancies. Nano Lett 13(4):1468–1475. https://doi.org/10.1021/nl304495v

60. Lin Y-C, Teng P-Y, Yeh C-H, Koshino M, Chiu P-W, Suenaga K (2015) Structural and chemical dynamics of pyridinic-nitrogen defects in graphene. Nano Lett 15(11):7408–7413. https://doi.org/10.1021/acs.nanolett.5b02831

61. Susi T, Kotakoski J, Kepaptsoglou D, Mangler C, Lovejoy TC, Krivanek OL, Zan R, Bangert U, Ayala P, Meyer JC, Ramasse Q (2014) Silicon-Carbon bond inversions driven by 60-keV electrons in graphene. Phys Rev Lett 113(11):115501. https://doi.org/10.1103/PhysRevLett.113.115501

62. Yang Z, Yin L, Lee J, Ren W, Cheng H-M, Ye H, Pantelides ST, Pennycook SJ, Chisholm MF (2014) Direct observation of atomic dynamics and silicon doping at a topological defect in graphene. Angew Chem Int Ed 53(34):8908–8912. https://doi.org/10.1002/anie.201403382

63. Meyer JC, Kisielowski C, Erni R, Rossell MD, Crommie MF, Zettl A (2008) Direct imaging of lattice atoms and topological defects in graphene membranes. Nano Lett 8(11):3582–3586. https://doi.org/10.1021/nl801386m

64. Li L, Reich S, Robertson J (2005) Defect energies of graphite: Density-functional calculations. Phys Rev B 72(18):184109. https://doi.org/10.1103/PhysRevB.72.184109

65. Kurasch S, Kotakoski J, Lehtinen O, Skákalová V, Smet J, Krill CE, Krasheninnikov AV, Kaiser U (2012) Atom-by-Atom observation of grain boundary migration in graphene. Nano Lett 12(6):3168–3173. https://doi.org/10.1021/nl301141g

66. Lin Y-C, Björkman T, Komsa H-P, Teng P-Y, Yeh C-H, Huang F-S, Lin K-H, Jadczak J, Huang Y-S, Chiu P-W (2015) Three-fold rotational defects in two-dimensional transition metal dichalcogenides. Nat Commun 6:6736. https://doi.org/10.1038/ncomms7736

67. Kotakoski J, Krasheninnikov A, Kaiser U, Meyer J (2011) From point defects in graphene to two-dimensional amorphous carbon. Phys Rev Lett 106(10):105505. https://doi.org/10.1103/PhysRevLett.106.105505

68. Chen Q, Robertson AW, He K, Gong C, Yoon E, Lee G-D, Warner JH (2015) Atomic level distributed strain within graphene divacancies from bond rotations. ACS Nano 9(8):8599–8608. https://doi.org/10.1021/acsnano.5b03801

69. Robertson AW, Lee G-D, He K, Yoon E, Kirkland AI, Warner JH (2014) Stability and dynamics of the tetravacancy in graphene. Nano Lett 14(3):1634–1642. https://doi.org/10.1021/nl500119p

70. Börrnert F, Avdoshenko SM, Bachmatiuk A, Ibrahim I, Büchner B, Cuniberti G, Rümmeli MH (2012) Amorphous carbon under 80 kV electron Irradiation: a means to make or break Graphene. Adv Mater 24(41):5630–5635. https://doi.org/10.1002/adma.201202173

71. Chuvilin A, Kaiser U, Bichoutskaia E, Besley NA, Khlobystov AN (2010) Direct transformation of graphene to fullerene. Nat Chem 2(6):450–453. https://doi.org/10.1038/nchem.644

72. Banhart F, Füller T, Redlich P, Ajayan PM (1997) The formation, annealing and self-compression of carbon onions under electron irradiation. Chem Phys Lett 269(3):349–355. https://doi.org/10.1016/S0009-2614(97)00269-8

73. Sun L, Rodriguez-Manzo J, Banhart F (2006) Elastic deformation of nanometer-sized metal crystals in graphitic shells. Appl Phys Lett 89(26):263104. https://doi.org/10.1063/1.2403898

74. Hiraki J, Mori H, Taguchi E, Yasuda H, Kinoshita H, Ohmae N (2005) Transformation of diamond nanoparticles into onion-like carbon by electron irradiation studied directly inside an ultrahigh-vacuum transmission electron microscope. Appl Phys Lett 86(22):223101. https://doi.org/10.1063/1.1935047

75. Lyutovich Y, Banhart F (1999) Low-pressure transformation of graphite to diamond under irradiation. Appl Phys Lett 74(5):659–660. https://doi.org/10.1063/1.122978

76. Zheng H, Rivest JB, Miller TA, Sadtler B, Lindenberg A, Toney MF, Wang L-W, Kisielowski C, Alivisatos AP (2011) Observation of transient structural-transformation dynamics in a Cu_2S nanorod. Science 333(6039):206–209. https://doi.org/10.1126/science.1204713

77. Lin Y-C, Dumcenco DO, Huang Y-S, Suenaga K (2014) Atomic mechanism of the semiconducting-to-metallic phase transition in single-layered MoS_2. Nat Nanotechnol 9(5):391–396. https://doi.org/10.1038/nnano.2014.64

78. Peng H, Meng W, Zheng H, Wei Y, Sheng H, Liu H, Li L, Wen G, Jia S, Li L, Wang J (2019) Probing the crystal and electronic structures of molybdenum oxide in redox process: implications for energy applications. ACS Appl Energy Mater 2(10):7709–7716. https://doi.org/10.1021/acsaem.9b01747

79. Zhao P, Cao F, Jia S, Zheng H, Wang J, Zhao D (2017) Phase transition of MoO_3 nanobelts under external fields. J Chin Electron Microsc Soc 36(5):429–435. https://doi.org/10.3969/j.issn.1000-6281.2017.05.002

80. Wang Y, Wen G, Li L, Liu H, Peng H, Jiang R, Zhuang Y, Jia S, Zheng H, Wang J (2019) Electron-beam-induced Growth and Reduction of $WO_{2.72}$ Single Crystal. J Chin Electron Microsc Soc 38(6):600–607. https://doi.org/10.3969/j.issn.1000-6281.2019.06.004

81. Jia S, Li L, Zhao L, Zheng H, Zhao P, Guan X, Chen G, Wu J, Zhou S, Wang J (2018) Surface-dependent formation of Zn clusters in ZnO single crystals by electron irradiation. Physical Review Materials 2(6):060402. https://doi.org/10.1103/PhysRevMaterials.2.060402

82. Sutter E, Huang Y, Komsa HP, Ghorbani-Asl M, Krasheninnikov AV, Sutter P (2016) Electron-Beam induced transformations of layered Tin Dichalcogenides. Nano Lett 16(7):4410–4416. https://doi.org/10.1021/acs.nanolett.6b01541

83. Lin J, Zuluaga S, Yu P, Liu Z, Pantelides ST, Suenaga K (2017) Novel Pd_2Se_3 Two-Dimensional phase driven by interlayer fusion in layered $PdSe_2$. Phys Rev Lett 119(1):016101. https://doi.org/10.1103/PhysRevLett.119.016101

84. Zhang H, Wang W, Xu T, Xu F, Sun L (2020) Phase transformation at controlled locations in nanowires by in situ electron irradiation. Nano Res 13(7):1912–1919. https://doi.org/10.1007/s12274-020-2711-2

85. Cao F, Zheng H, Jia S, Bai X, Li L, Sheng H, Wu S, Han W, Li M, Wen G, Yu J, Wang J (2015) Atomistic observation of phase transitions in calcium sulfates under electron irradiation. The Journal of Physical Chemistry C 119(38):22244–22248. https://doi.org/10.1021/acs.jpcc.5b07508

86. Chen S, Zhang X, Zhao J, Zhang Y, Kong G, Li Q, Li N, Yu Y, Xu N, Zhang J, Liu K, Zhao Q, Cao J, Feng J, Li X, Qi J, Yu D, Li J, Gao P (2018) Atomic scale insights into structure instability and decomposition pathway of methylammonium lead iodide perovskite. Nat Commun 9(1):4807. https://doi.org/10.1038/s41467-018-07177-y

87. Wei X, Wang M-S, Bando Y, Golberg D (2011) Electron-Beam-Induced substitutional carbon doping of boron nitride nanosheets, nanoribbons, and nanotubes. ACS Nano 5(4):2916–2922. https://doi.org/10.1021/nn103548r

88. Sun L, Banhart F (2006) Graphitic onions as reaction cells on the nanoscale. Appl Phys Lett 88(19):193121. https://doi.org/10.1063/1.2202106

89. Sheng H, Zheng H, Jia S, Chan MK, Rajh T, Wang J, Wen J (2019) Atomistic manipulation of reversible oxidation and reduction in Ag with an electron beam. Nanoscale 11(22):10756–10762. https://doi.org/10.1039/C8NR09525F

90. Zheng H, Wu S, Sheng H, Liu C, Liu Y, Cao F, Zhou Z, Zhao X, Zhao D, Wang J (2014) Direct atomic-scale observation of layer-by-layer oxide growth during magnesium oxidation. Appl Phys Lett 104(14):141906. https://doi.org/10.1063/1.4870832

91. Cao F, Zheng H, Jia S, Liu H, Li L, Chen B, Liu X, Wu S, Sheng H, Xing R (2016) Atomistic observation of structural evolution during magnesium oxide growth. J Phys Chem C 120(47):26873–26878. https://doi.org/10.1021/acs.jpcc.6b08833

92. Meng S, Wu J, Zhao L, Zheng H, Jia S, Hu S, Meng W, Pu S, Zhao D, Wang J (2018) Atomistic insight into the redox reactions in Fe/Oxide Core-Shell nanoparticles. Chem Mater 30(20):7306–7312. https://doi.org/10.1021/acs.chemmater.8b03679

93. Su Q, Du G, Xu B (2014) In situ growth of In_2O_3 nanocrystals by electron irradiation in transmission electron microscope. Mater Lett 120:208–211. https://doi.org/10.1016/j.matlet.2014.01.068

94. Gonzalez-Martinez I, Bachmatiuk A, Bezugly V, Kunstmann J, Gemming T, Liu Z, Cuniberti G, Rümmeli M (2016) Electron-beam induced synthesis of nanostructures: a review. Nanoscale 8(22):11340–11362. https://doi.org/10.1039/C6NR01941B

95. Du X-w, Takeguchi M, Tanaka M, Furuya K (2003) Formation of crystalline Si nanodots in SiO2 films by electron irradiation. Appl Phys Lett 82(7):1108–1110. https://doi.org/10.1063/1.1555691

96. Yu K, Xu T, Wu X, Wang W, Zhang H, Zhang Q, Tang L, Sun L (2019) In Situ Observation of Crystalline Silicon Growth from SiO₂ at Atomic Scale. Research 2019:3289247. https://doi.org/10.34133/2019/3289247

97. Gonzalez-Martinez IG, Gorantla SM, Bachmatiuk A, Bezugly V, Zhao J, Gemming T, Kunstmann J, Jr E, Cuniberti G, Rümmeli MH (2014) Room temperature in situ growth of B/BO x nanowires and BO x nanotubes. Nano Lett 14(2):799–805. https://doi.org/10.1021/nl404147r

98. Jia S, Hu S, Zheng H, Wei Y, Meng S, Sheng H, Liu H, Zhou S, Zhao D, Wang J (2018) Atomistic interface dynamics in Sn-Catalyzed growth of Wurtzite and Zinc-Blende ZnO nanowires. Nano Lett 18(7):4095–4099. https://doi.org/10.1021/acs.nanolett.8b00420

99. Edmondson MJ, Zhou W, Sieber S, Jones I, Gameson I, Anderson P, Edwards P (2001) Electron-Beam induced growth of bare silver nanowires from zeolite crystallites. Adv Mater 13(21):1608–1611. https://doi.org/10.1002/1521-4095(200111)13:21%3C1608::AID-ADMA1608%3E3.0.CO;2-S

100. Rodríguez-Manzo JA, Terrones M, Terrones H, Kroto HW, Sun L, Banhart F (2007) In situ nucleation of carbon nanotubes by the injection of carbon atoms into metal particles. Nat Nanotechnol 2(5):307–311. https://doi.org/10.1038/nnano.2007.107

101. Sang X, Xie Y, Yilmaz DE, Lotfi R, Alhabeb M, Ostadhossein A, Anasori B, Sun W, Li X, Xiao K, Kent PRC, van Duin ACT, Gogotsi Y, Unocic RR (2018) In situ atomistic insight into the growth mechanisms of single layer 2D transition metal carbides. Nat Commun 9(1):2266. https://doi.org/10.1038/s41467-018-04610-0

102. Zheng H, Liu Y, Cao F, Wu S, Jia S, Cao A, Zhao D, Wang J (2013) Electron beam-assisted healing of nanopores in magnesium alloys. Sci Rep 3(1):1920. https://doi.org/10.1038/srep01920

103. Shen Y, Xu T, Tan X, He L, Yin K, Wan N, Sun L (2018) In Situ Repair of 2D chalcogenides under electron beam irradiation. Adv Mater 30(14):1705954. https://doi.org/10.1002/adma.201705954

104. Zhao J, Deng Q, Bachmatiuk A, Sandeep G, Popov A, Eckert J, Rümmeli MH (2014) Free-Standing Single-Atom-Thick Iron membranes suspended in graphene pores. Science 343(6176):1228–1232. https://doi.org/10.1126/science.1245273

105. Yin K, Zhang YY, Zhou Y, Sun L, Chisholm MF, Pantelides ST, Zhou W (2017) Unsupported single-atom-thick copper oxide monolayers. 2D Materials 4(1):011001. https://doi.org/10.1088/2053-1583/4/1/011001

106. Wan N, Xu J, Xu T, Matteo M, Sun L, Sun J, Zhou Y (2013) Surface energy guided sub-10 nm hierarchy structures fabrication by direct e-beam etching. RSC Adv 3(39):17860–17865. https://doi.org/10.1039/c3ra42370k

107. Shen Y, Xu T, Tan X, Sun J, He L, Yin K, Zhou Y, Banhart F, Sun L (2017) Electron beam etching of CaO crystals observed atom by atom. Nano Lett 17(8):5119–5125. https://doi.org/10.1021/acs.nanolett.7b02498

108. Tang L, He L, Zhang L, Yu K, Xu T, Zhang Q, Dong H, Zhu C, Sun L (2018) A novel domain-confined growth strategy for in situ controllable fabrication of individual hollow nanostructures. Advanced Science 5(5):1700213. https://doi.org/10.1002/advs.201700213

109. Wu S, Zheng H, Jia S, Sheng H, Cao F, Li L, Hu S, Zhao P, Zhao D, Wang J (2016) Three-dimensional structures of magnesium nanopores. Nanotechnology 27(12):125603. https://doi.org/10.1088/0957-4484/27/12/125603

110. Wu S, Cao F, Zheng H, Sheng H, Liu C, Liu Y, Zhao D, Wang J (2013) Fabrication of faceted nanopores in magnesium. Appl Phys Lett 103(24):243101. https://doi.org/10.1063/1.4841515

111. Xu T, Yin K, Xie X, He L, Wang B, Sun L (2012) Size-dependent evolution of graphene nanopores under thermal excitation. Small 8(22):3422–3426. https://doi.org/10.1002/smll.201200979

112. Kondo Y, Takayanagi K (1997) Gold nanobridge stabilized by surface structure. Phys Rev Lett 79(18):3455. https://doi.org/10.1103/PhysRevLett.79.3455

113. Kondo Y, Takayanagi K (2000) Synthesis and characterization of helical multi-shell gold nanowires. Science 289(5479):606–608. https://doi.org/10.1126/science.289.5479.606

114. Rodrigues V, Fuhrer T, Ugarte D (2000) Signature of atomic structure in the quantum conductance of gold nanowires. Phys Rev Lett 85(19):4124. https://doi.org/10.1103/PhysRevLett.85.4124

115. Rodrigues V, Bettini J, Rocha A, Rego LG, Ugarte D (2002) Quantum conductance in silver nanowires: Correlation between atomic structure and transport properties. Phys Rev B 65(15):153402. https://doi.org/10.1103/PhysRevB.65.153402

116. González JC, Rodrigues V, Bettini J, Rego LGC, Rocha AR, Coura PZ, Dantas SO, Sato F, Galvão DS, Ugarte D (2004) Indication of unusual pentagonal structures in atomic-size cu nanowires. Phys Rev Lett 93(12):126103. https://doi.org/10.1103/PhysRevLett.93.126103

117. Rodrigues V, Sato F, Galvão DS, Ugarte D (2007) Size limit of defect formation in pyramidal Pt nanocontacts. Phys Rev Lett 99(25):255501. https://doi.org/10.1103/PhysRevLett.99.255501

118. Jin C, Lan H, Peng L, Suenaga K, Iijima S (2009) Deriving carbon atomic chains from graphene. Phys Rev Lett 102(20):205501. https://doi.org/10.1103/PhysRevLett.102.205501

119. La Torre A, Botello-Mendez A, Baaziz W, Charlier JC, Banhart F (2015) Strain-induced metal–semiconductor transition observed in atomic carbon chains. Nat Commun 6:6636. https://doi.org/10.1038/ncomms7636

120. Lin Y-C, Morishita S, Koshino M, Yeh C-H, Teng P-Y, Chiu P-W, Sawada H, Suenaga K (2017) Unexpected huge dimerization ratio in one-dimensional carbon atomic Chains. Nano Lett 17(1):494–500. https://doi.org/10.1021/acs.nanolett.6b04534

121. Cretu O, Komsa H-P, Lehtinen O, Algara-Siller G, Kaiser U, Suenaga K, Krasheninnikov AV (2014) Experimental observation of boron nitride Chains. ACS Nano 8(12):11950–11957. https://doi.org/10.1021/nn5046147

122. Xiao Z, Qiao J, Lu W, Ye G, Chen X, Zhang Z, Ji W, Li J, Jin C (2017) Deriving phosphorus atomic chains from few-layer black phosphorus. Nano Res 10(7):2519–2526. https://doi.org/10.1007/s12274-017-1456-z

123. Liu X, Xu T, Wu X, Zhang Z, Yu J, Qiu H, Hong J-H, Jin C-H, Li J-X, Wang X-R, Sun L-T, Guo W (2013) Top-down fabrication of sub-nanometre semiconducting nanoribbons derived from molybdenum disulfide sheets. Nat Commun 4:1776. https://doi.org/10.1038/ncomms2803

124. Lin J, Cretu O, Zhou W, Suenaga K, Prasai D, Bolotin KI, Cuong NT, Otani M, Okada S, Lupini AR (2014) Flexible metallic nanowires with self-adaptive contacts to semiconducting transition-metal dichalcogenide monolayers. Nat Nanotechnol 9(6):436–442. https://doi.org/10.1038/nnano.2014.81

125. Lin J, Zhang Y, Zhou W, Pantelides ST (2016) Structural flexibility and alloying in ultrathin transition-metal chalcogenide nanowires. ACS Nano 10(2):2782–2790. https://doi.org/10.1021/acsnano.5b07888

126. Xu T, Zhou Y, Tan X, Yin K, He L, Banhart F, Sun L (2017) Creating the smallest BN nanotube from bilayer h-BN. Adv Func Mater 27(19):1603897. https://doi.org/10.1002/adfm.201603897

127. Li J, Banhart F (2005) The deformation of single, nanometer-sized metal crystals in graphitic shells. Adv Mater 17(12):1539–1542. https://doi.org/10.1002/adma.200401917

128. Banhart F, Charlier J-C, Ajayan P (2000) Dynamic behavior of nickel atoms in graphitic networks. Phys Rev Lett 84(4):686. https://doi.org/10.1103/PhysRevLett.84.686

129. Sun L, Krasheninnikov AV, Ahlgren T, Nordlund K, Banhart F (2008) Plastic deformation of single nanometer-sized crystals. Phys Rev Lett 101(15):156101. https://doi.org/10.1103/PhysRevLett.101.156101

130. Sun L, Banhart F, Krasheninnikov A, Rodriguez-Manzo J, Terrones M, Ajayan P (2006) Carbon nanotubes as high-pressure cylinders and nanoextruders. Science 312(5777):1199–1202. https://doi.org/10.1126/science.1124594

131. Lagos M, Sato F, Bettini J, Rodrigues V, Galvao DS, Ugarte D (2009) Observation of the smallest metal nanotube with a square cross-section. Nat Nanotechnol 4(3):149–152. https://doi.org/10.1038/NNANO.2008.414

132. Zhao P, Guan X, Zheng H, Jia S, Li L, Liu H, Zhao L, Sheng H, Meng W, Zhuang Y (2019) Surface-and strain-mediated reversible phase transformation in quantum-confined ZnO nanowires. Phys Rev Lett 123(21):216101. https://doi.org/10.1103/PhysRevLett.123.216101
133. Chen Q, Dwyer C, Sheng G, Zhu C, Li X, Zheng C, Zhu Y (2020) Imaging Beam-Sensitive materials by electron microscopy. Adv Mater 32:1907619. https://doi.org/10.1002/adma.201907619